Science of Remote Sensing 10 (2024) 100169

Contents lists available at ScienceDirect

Science of Remote Sensing

journal homepage: www.sciencedirect.com/journal/science-of-remote-sensing

Design and performance of the Climate Change Initiative Biomass global retrieval algorithm

Maurizio Santoro [a,*], Oliver Cartus [a], Shaun Quegan [b], Heather Kay [c], Richard M. Lucas [c], Arnan Araza [d], Martin Herold [d,e], Nicolas Labrière [f], Jérôme Chave [f], Åke Rosenqvist [g], Takeo Tadono [h], Kazufumi Kobayashi [i], Josef Kellndorfer [j], Valerio Avitabile [k], Hugh Brown [l], João Carreiras [b], Michael J. Campbell [m], Jura Cavlovic [n], Polyanna da Conceição Bispo [o], Hammad Gilani [p], Mohammed Latif Khan [q], Amit Kumar [r,u], Simon L. Lewis [s,t], Jingjing Liang [u], Edward T.A. Mitchard [v], Ana María Pacheco-Pascagaza [o,w], Oliver L. Phillips [t], Casey M. Ryan [v], Purabi Saikia [x], Dmitry Schepaschenko [y], Hansrajie Sukhdeo [z], Hans Verbeeck [aa], Ghislain Vieilledent [ab], Arief Wijaya [ac], Simon Willcock [ad,ae], Frank Martin Seifert [af]

[a] *Gamma Remote Sensing, Worbstasse 225, 3073, Gümligen, Switzerland*
[b] *National Centre for Earth Observation (NCEO), University of Sheffield, Sheffield, S3 7RH, United Kingdom*
[c] *Department of Geography and Earth Sciences, Aberystwyth University, Aberystwyth, SY23 3DB, United Kingdom*
[d] *Laboratory of Geo-Information Science and Remote Sensing, Wageningen University & Research, Droevendaalsesteeg 3, 6708 PB, Wageningen, the Netherlands*
[e] *Helmholtz GFZ German Research Centre for Geosciences, Remote Sensing and Geoinformatics Section, Telegrafenberg, Potsdam, Germany*
[f] *Centre de Recherche sur la Biodiversité et l'Environnement, UMR 5300 (CNRS/IRD/UPS/INPT), 31062 Toulouse, Cedex 9, France*
[g] *solo Earth Observation, Kachidoki 6-3-2, Chuo-ku, Tokyo, 104-0054, Japan*
[h] *Japan Aerospace Exploration Agency, Earth Observation Research Center, Tsukuba-shi, Ibaraki-ken, 305-8505, Japan*
[i] *Remote Sensing Technology Center of Japan, Tokyu Reit Toranomon Bldg 3F, 3-17-1 Toranomon, Minato-ku, Tokyo, 105-0001, Japan*
[j] *Earth Big Data LLC, P.O. Box 114, Woods Hole, MA, 02543, USA*
[k] *European Commission, Joint Research Centre, Ispra, Italy*
[l] *University of Helsinki, Department of Forest Science, 00790, Helsinki, Finland*
[m] *School of Environment, Society and Sustainability, University of Utah, USA*
[n] *University of Zagreb, Faculty of Forestry and Wood Technology, Department of Forest Inventory and Management, Croatia*
[o] *Department of Geography, School of Environment, Education and Development, University of Manchester, Oxford Rd., Manchester, M13 9PL, United Kingdom*
[p] *Plant and Environmental Sciences, New Mexico State University, Las Cruces, NM 88003, USA*
[q] *Dr. Harisingh Gour Vishwavidyalaya (A Central University), Sagar, Madhya Pradesh, India*
[r] *Department of Geography, Sikkim University, Gangtok, 737102, India*
[s] *Department of Geography, University College London, London, WC1E 6BT, United Kingdom*
[t] *School of Geography, University of Leeds, Woodhouse Lane, Leeds, LS2 9JT, United Kingdom*
[u] *Department of Forestry and Natural Resources, Purdue University, 715 W State St, West Lafayette, IN 47907, USA*
[v] *University of Edinburgh, School of GeoSciences, Crew Building, The King's Buildings, Edinburgh, EH9 3FF, United Kingdom*
[w] *Satellite Applications Catapult, Didcot, OX11 0QR, United Kingdom*
[x] *Department of Botany, Banaras Hindu University, Varanasi, 221005, India*
[y] *International Institute for Applied Systems Analysis, Schlossplatz 1, A-2361, Laxenburg, Austria*
[z] *Guyana Forestry Commission, 1 Water Street Kingston, Georgetown, Guyana*
[aa] *CAVElab – Computational and Applied Vegetation Ecology, Department of Environment, Ghent University, Coupure Links 653, 9000, Gent, Belgium*
[ab] *AMAP, University of Montpellier, CIRAD, CNRS, INRAE, IRD, Montpellier, France*

* Corresponding author.
E-mail addresses: santoro@gamma-rs.ch (M. Santoro), cartus@gamma-rs.ch (O. Cartus), S.Quegan@sheffield.ac.uk (S. Quegan), hek4@aber.ac.uk (H. Kay), richard.lucas@aber.ac.uk (R.M. Lucas), arnan.araza@wur.nl (A. Araza), herold@gfz-potsdam.de (M. Herold), nicolas.labriere@gmail.com (N. Labrière), jerome.chave@univ-tlse3.fr (J. Chave), ake.rosenqvist@soloeo.com (Å. Rosenqvist), tadono.takeo@jaxa.jp (T. Tadono), kobayashi_kazufumi@restec.jp (K. Kobayashi), josef@earthbigdata.com (J. Kellndorfer), vavi.work@gmail.com (V. Avitabile), hughbrown03@hotmail.com (H. Brown), j.carreiras@sheffield.ac.uk (J. Carreiras), mickey.campbell@geog.utah.edu (M.J. Campbell), jcavlovic@sumfak.hr (J. Cavlovic), polyanna.bispo@manchester.ac.uk (P.C. Bispo), hammad.gilani@gmail.com (H. Gilani), khanml61@gmail.com (M.L. Khan), amit.iirs@gmail.com, amit.kumar@cuj.ac.in (A. Kumar), s.l.lewis@ucl.ac.uk (S.L. Lewis), jjliang@purdue.edu (J. Liang), edward.mitchard@ed.ac.uk (E.T.A. Mitchard), anamaria.pacheco@sa.catapult.org.uk (A.M. Pacheco-Pascagaza), O.Phillips@leeds.ac.uk (O.L. Phillips), casey.ryan@ed.ac.uk (C.M. Ryan), purabi.saikia83@gmail.com (P. Saikia), schepd@iiasa.ac.at (D. Schepaschenko), hans.sukhdeo@gmail.com (H. Sukhdeo), Hans.Verbeeck@UGent.be (H. Verbeeck), ghislain.vieilledent@cirad.fr (G. Vieilledent), Arief.Wijaya@wri.org (A. Wijaya), s.willcock@bangor.ac.uk (S. Willcock), Frank.Martin.Seifert@esa.int (F.M. Seifert).

https://doi.org/10.1016/j.srs.2024.100169
Received 16 July 2024; Received in revised form 20 September 2024; Accepted 29 September 2024
Available online 30 September 2024

[ac] Research and Data Integrity Department, World Resources Institute Indonesia, Jl Wijaya I/63, South Jakarta, Indonesia
[ad] School of Environmental and Natural Sciences, Bangor University, LL57 2UR, United Kingdom
[ae] Net Zero and Resilient Farming, Rothamsted Research, West Common, Harpenden, AL5 2JQ, United Kingdom
[af] European Space Research Institute, European Space Agency, 00044, Frascati, Italy

ARTICLE INFO

Keywords:
Above-ground biomass
Carbon
Forest
Synthetic Aperture Radar
Backscatter
Sentinel-1
ALOS-2 PALSAR-2
LiDAR
ICESat GLAS
ICESat-2 ATLAS
Retrieval

ABSTRACT

The increase in Earth observations from space in recent years supports improved quantification of carbon storage by terrestrial vegetation and fosters studies that relate satellite measurements to biomass retrieval algorithms. However, satellite observations are only indirectly related to the carbon stored by vegetation. While ground surveys provide biomass stock measurements to act as reference for training the models, they are sparsely distributed. Here, we addressed this problem by designing an algorithm that harnesses the interplay of satellite observations, modeling frameworks and field measurements, and generated global estimates of above-ground biomass (AGB) density that meet the requirements of the scientific community in terms of accuracy, spatial and temporal resolution. The design was adapted to the amount, type and spatial distribution of satellite data available around the year 2020. The retrieval algorithm estimated AGB annually by merging estimates derived from C- and L-band Synthetic Aperture Radar (SAR) backscatter observations with a Water Cloud type of model and does not rely on AGB reference data at the same spatial scale as the SAR data. This model is integrated with functions relating to forest structural variables that were trained on spaceborne LiDAR observations and sub-national AGB statistics. The yearly estimates of AGB were successively harmonized using a cost function that minimizes spurious fluctuations arising from the moderate-to-weak sensitivity of the SAR backscatter to AGB. The spatial distribution of the AGB estimates was correctly reproduced when the retrieval model was correctly set. Over-predictions occasionally occurred in the low AGB range (<50 Mg ha^{-1}) and under-predictions in the high AGB range (>300 Mg ha^{-1}). These errors were a consequence of sometimes too strong generalizations made within the modeling framework to allow reliable retrieval worldwide at the expense of accuracy. The precision of the estimates was mostly between 30% and 80% relative to the estimated value. While the framework is well founded, it could be improved by incorporating additional satellite observations that capture structural properties of vegetation (e.g., from SAR interferometry, low-frequency SAR, or high-resolution observations), a dense network of regularly monitored high-quality forest biomass reference sites, and spatially more detailed characterization of all model parameters estimates to better reflect regional differences.

1. Introduction

Above-ground biomass is defined by the Global Carbon Observing System (GCOS) as one of 55 Essential Climate Variables (ECV) due to its impacts on the surface energy budget, the land surface water balance, the atmospheric concentration of greenhouse gases and a range of ecosystem services, such as provision of timber and recreation. AGB is defined as the mass, expressed as oven-dry weight of the woody parts (stem, bark, branches, and twigs), of all living trees excluding stump and roots and is directly related to the amount of carbon stored by the woody vegetation. In this study, AGB refers to the density of biomass per unit area and is expressed in Mg ha^{-1}.

Quantifying the amount of biomass stored in live vegetation globally requires techniques that can collect data related to biomass in a timely and reliable manner (Houghton et al., 2009). Surveys implemented in forest inventories are designed to cover large areas with high precision in a timely and cost-effective manner while Earth Observation (EO) from space achieves wall-to-wall coverage within days to weeks and captures the spatial variability of biomass (Goetz et al., 2009). However, as neither the carbon content nor the organic mass stored in woody vegetation can be measured by EO, such data need to be ingested in modelling frameworks that estimate biomass.

The availability of global and repeated image datasets acquired by satellites led to the first wall-to-wall datasets of AGB in the early 2010s (Baccini et al., 2012; Hu et al., 2016; Saatchi et al., 2011). The lack of extensive field observations of AGB to train the retrieval model was overcome by using the spatially dense global dataset of Ice Cloud and Elevation Satellite (ICESat) observations together with models that predicted AGB from ICESat metrics. AGB retrieval models, whose predictors came from EO image datasets, were then trained with these samples and inverted to create wall-to-wall maps of AGB.

Regardless of the reference dataset, AGB was predicted over large areas with a single model parameterization (Bouvet et al., 2018). The resulting failure to capture spatial changes in the relationship between AGB and the predictor variables caused biases (Avitabile et al., 2011; Bouvet et al., 2018; Mitchard et al., 2013). Finer stratification of the models relating LiDAR metrics to field measurements of AGB was therefore introduced with the availability of AGB maps inferred from regional Airborne Laser Scanning (ALS) campaigns (Xu et al., 2017, 2021). Such maps are based on dense spatial sampling and accurate measurements of canopy structure metrics, so the relationship between AGB from field plots and the LiDAR observations is well characterized (Ferraz et al., 2018; Labriere et al., 2018; Ometto et al., 2023; Xu et al., 2017). However, the uneven spatial distribution of ALS-based maps of AGB may cause biases if the statistical relationships between AGB and LiDAR-derived metrics, such as mean canopy height, are extended to areas where they have not been validated.

A straightforward procedure to compensate for the lack of widespread reference AGB observations to train a retrieval model is to use existing wall-to-wall AGB map estimates (Chen et al., 2021; Fan et al., 2019; Liu et al., 2015; Prigent and Jimenez, 2021) or spatially dense estimates of AGB from spaceborne LiDAR (Shendryk, 2022). Model training can account for spatial variability in how the EO signals respond to AGB but it may propagate biases in the map-based AGB values (Salazar-Neira et al., 2023) into the derived AGB retrieval model.

Given an extensive dataset of reference samples, the retrieval model can be based either on a global regression equation (Fan et al., 2019; Liu et al., 2015) or a non-parametric approach (Prigent and Jimenez, 2021; Salazar-Neira et al., 2023; Shendryk, 2022). A parametric approach requires knowledge of the signatures of the EO predictors (Liu et al., 2015; Rodríguez-Fernández et al., 2018). The retrieval model can then be tailored to the AGB reference values, e.g., by stratification according to ecological or geographical criteria. Usually, only a few model realizations are used to cover the globe, which leads to strong generalization in the retrieval model. Machine learning instead offers a means of adapting the relationship between AGB and the EO data to local conditions; it may also mitigate deficiencies in the reference dataset when multiple predictors are used (Salazar-Neira et al., 2023).

Nonetheless, while the reasons for errors from a parametric model can be identified and fixed, the trial-and-error approach underlying machine learning hinders this type of insight.

Having the aim of estimating AGB globally with a spatial resolution of 1 ha for 2010, Santoro et al. (2021a) addressed these issues by: (i) using a parametric modeling framework; (ii) adopting a spatially adaptive procedure to estimate the parameters of the retrieval model; and (iii) removing the requirement for training data. The retrieval algorithm had to be built around global EO image data for that epoch that were sensitive to forest structural properties. This requirement was met by Synthetic Aperture Radar (SAR) observations of backscattered intensity at C-band (multiple observations) and L-band (single observation). Calibration of the SAR-based retrieval model was aided by maps of forest variables derived from optical satellite images. The overall spatial distribution of AGB was captured but with positive biases for lower AGB (50–100 Mg ha^{-1}) and negative biases in the high AGB range (>250 Mg ha^{-1}) (Santoro et al., 2021a). Retrieval errors were explained as a consequence of concurring factors: (i) lack of sensitivity of SAR backscatter to biomass in the upper range of AGB; (ii) a broad empirical approach to modelling the interaction between microwaves and forest structure; (iii) too few observations from satellites; (iv) incorrect assumptions on the range of AGB that could be estimated at a given location; and (v) artefacts in the satellite data.

While the effect of the sensitivity of the SAR backscatter to AGB cannot be compensated for, all other causes of bias can be dealt with. Systematic and repeated observations by the wider range of spaceborne SAR and LiDAR instruments onboard more recent missions and substantial advances in modelling the relationship between AGB and spaceborne LiDAR metrics of forest structure (Duncanson et al., 2022; Kay et al., 2021; Labriere et al., 2018) permit major improvements to global retrieval algorithms that follow the approach developed by Santoro et al. (2021a).

Compared to this study, we exploit a denser set of LiDAR observations and of SAR images that have stronger sensitivity to AGB (multi-temporal L-band and cross-polarized C-band backscatter data). The retrieval model shifts from using just a few empirical functions to incorporating LiDAR data, which support two structural functions that provide a fully parametric explanation of the link between SAR backscatter and AGB. Additionally, the availability of several years of SAR data allow to introduce the temporal dimension in the process of merging AGB estimates from the different SAR data streams to stabilize its estimation. These innovations yield a global AGB retrieval approach that is fully parametric and physics-based, and is designed to integrate multiple data streams at high-to-moderate spatial resolution (≤1 ha) from satellites which are operational over decades.

The approach is referred to as the CCI Biomass retrieval algorithm since it was developed within the European Space Agency Climate Change Initiative (Plummer et al., 2017). The performance of the retrieval algorithm is assessed here only for one year, since the focus of this paper is on the design and performance of the AGB retrieval method, and its accuracy is assessed by comparing against field measurements of AGB. While the algorithm is designed to create repeated estimates of AGB over several decades from which trends in AGB can be derived, comparison of the AGB estimates from this study with those from other global datasets and validation of AGB changes require additional investigations, which are deferred to a later paper.

2. Datasets

This Section provides an overview of the datasets used to either estimate AGB or to validate the estimates (Table 1). They comprise satellite observations by SAR and LiDAR missions (Sections 2.1 and 2.2), map products derived from satellite observations and other ancillary data (Section 2.3), and AGB values derived from field inventories (Section 2.4). As the satellite measurements are only partly related to the mass of the trees and have intrinsic errors, the spatial resolution of the AGB estimates was set to 100 m × 100 m, which is coarser than the spatial resolution of any predictor variable but still acceptable for discerning spatial patterns in the AGB maps. This resolution was obtained by spatial averaging or resampling each dataset before their use in the retrieval. This both increases the radiometric and geometric quality of the data and reduces the computing resources needed to generate global, spatially explicit estimates of AGB.

Table 1
List of datasets used to estimate AGB with the proposed retrieval algorithm. The spatial scale refers to the pixel size of the dataset as used by the biomass retrieval algorithm.

Dataset	Observable	Use	Year	Spatial scale
ALOS-2 PALSAR-2	SAR backscatter	Predictor	2015–2021	100 m × 100 m
Sentinel-1	SAR backscatter	Predictor	2015–2021	150 m × 150 m
ICESat-1 GLAS	Canopy height and density	Predictor	2003–2009	70 m diameter
ICESat-2 ATLAS	Canopy height	Predictor	2019–2021	25 m × 100 m
Landsat tree cover	Canopy density	Auxiliary	2010	30 m × 30 m
CCI Land Cover	Land cover	Auxiliary	2015–2021	300 m × 300 m
Copernicus DEM	Surface elevation	Auxiliary	Ca. 2010	30 m × 30 m
Terrestrial Ecoregions of the World	Ecoregions, biomes and realms	Auxiliary	Undated	Polygons
Plot-level AGB	Values of AGB at field inventory plots	Validation	2020	Between 0.1 and 6 ha
Inventory-based AGB statistics	Subnational AGB average value from field inventory data	Predictor	2000–2020	(Sub)-national

The Advanced Land Observing Satellite (ALOS-2) Phased Array L-band SAR (PALSAR-2) data displayed stronger sensitivity to forest structure than other satellite image datasets (Santoro and Cartus, 2018) and represented the most important predictor of AGB. Although C-band microwaves have limited penetration into vegetation canopies, the Sentinel-1 C-band dataset was found to contribute in sparse and moderate forest cover. While spaceborne LiDAR observations can provide reliable descriptors of forest structure, they were available only as discrete samples, so were used as ancillary datasets supporting the AGB prediction. Thematic datasets of canopy density, land cover, terrain elevation and ecoregions were used to inform either the SAR pre-processing or training of the retrieval model.

Plot-level AGB estimates were used only for validation because their uneven worldwide distribution and differences in their measurement protocols prevented spatially consistent estimation of parameters of the AGB retrieval model. Reference AGB values were instead provided by average values from National Forest Inventory (NFI) data at subnational scale, which provided wide coverage at the expense of spatial detail.

2.1. SAR datasets

2.1.1. ALOS-2 PALSAR-2

The ALOS-2 PALSAR-2 instrument operates at L-band (wavelength: 23.5 cm) in several modes. We used images acquired in Fine Beam (FB) and Wide Beam (WB) modes. Data were acquired in dual polarization (HH and HV), covering swaths of approximately 70 km in FB mode and 350 km in WB mode. In FB mode, acquisitions are scheduled to maximize the information on land surface properties from given regions (Rosenqvist et al., 2014). The WB mode implements the ScanSAR imaging technique, which gives coverage of a larger swath at the expense of spatial resolution. An additional advantage of the wide swath is that

adjacent swaths overlap significantly (about 75% at the Equator, more at higher latitudes), allowing multiple observations within the satellite's revisit cycle of 14 days.

The FB and WB mode datasets consisted of all images acquired between 2015 and 2021. As part of the systematic observation plan implemented for ALOS-2 (https://www.eorc.jaxa.jp/ALOS/en/alos-2/a2_observation_e.htm), the FB images were acquired primarily between May and October, resulting in a small number of observations per location (pixel) (Fig. 1). The WB mode is operated primarily across the tropical belt, giving a higher density of measurements across the tropics, in places reaching 20 observations per pixel in 2020 (Fig. 1). The average SAR backscatter (Fig. 1) shows almost full global coverage with the two modes, with small gaps in northern Siberia and southeast China. The highest backscatter occurred in regions with large biomass stocks such as tropical rainforests in South America, Central Africa and Southeast Asia, and temperate and boreal forest across the northern hemisphere, the Andes, and Southeast Australia. In contrast, sparsely forested regions such as the Canadian Prairies, northern Siberia, the Pampas and the Australian Outback have low backscatter. The mosaic of PALSAR-2 images also shows banding corresponding to backscatter offsets between adjacent strips either along ascending orbits (e.g., in the boreal zone, imaged in the FB mode) or descending orbits (in the tropical zone, imaged more frequently in the WB mode). This arises from a combination of the dependence of the backscatter on local incidence angle, which differs depending on the scattering object, and imperfect calibration across the image swath of the FB and WB modes.

As part of the support by the Japan Aerospace Exploration Agency (JAXA) to the CCI Biomass project, a dedicated processing chain was established by JAXA with ALOS-2 FB data provided as extended backscatter path images with a pixel size of approximately 25 m × 25 m in the radar geometry. We pre-processed the path images to produce fully calibrated and terrain-corrected backscatter data with a pixel size of 100 m × 100 m (Fig. S1). The Noise Equivalent Sigma Zero (NESZ) in the original SAR images was first compensated, based on range gradients of backscatter over smooth water surfaces. Each image was then multi-looked with a 4 × 4 pixel window, and terrain geocoded with a look-up table relating the SAR and the map geometry represented in the Digital Elevation Model (DEM) (Section 2.3), before tiling to a predefined 1° × 1° grid. This tiling system was implemented to create stacks of co-registered observations from the various SAR backscatter datasets.

The look-up table supporting terrain geocoding was derived from ALOS-2 orbital data, elevation information in the DEM, and parameters of the SAR look geometry (Wegmüller, 1999). Images of local incidence angle, pixel area and a mask of layover and shadow were also obtained (Frey et al., 2013). The SAR images were then corrected for pixel area variations, including the conversion from s^0 to g^0 (i.e., σ^0 divided by the cosine of the local incidence angle), which accounted for the effect of local incidence angle on the SAR backscatter (Frey et al., 2013). Imperfections in the look-up table due to uncertainties in the parameters involved in its estimation were corrected by matching the SAR image to a SAR image simulated from the DEM (Wegmüller et al., 2002). The geocoding accuracy was estimated for each individual scene, resulting on average in a few tenths of the pixel size.

The ScanSAR data were pre-processed by JAXA and terrain-geocoded to geographic coordinates and a pixel size equivalent to 50 m at the Equator. The ALOS World 3D-30m (AW3D30) Digital Surface Model (DSM) created from data acquired by the Panchromatic Remote-sensing Instrument for Stereo Mapping (PRISM) onboard ALOS provided the reference for the elevation (Tadono et al., 2014). The images were also compensated for variations in the pixel scattering area due to topography and for the dependence of backscatter on the local incidence angle (Shimada and Ohtaki, 2010). The WB images were provided by JAXA in the form of 1° large tiles, each consisting of: (i) the co- and cross-polarized SAR backscatter images, (ii) an image of the local incidence angle with respect to the orientation of the pixel, derived from the DEM used by JAXA for the pre-processing, (iii) layover/shadow masks,

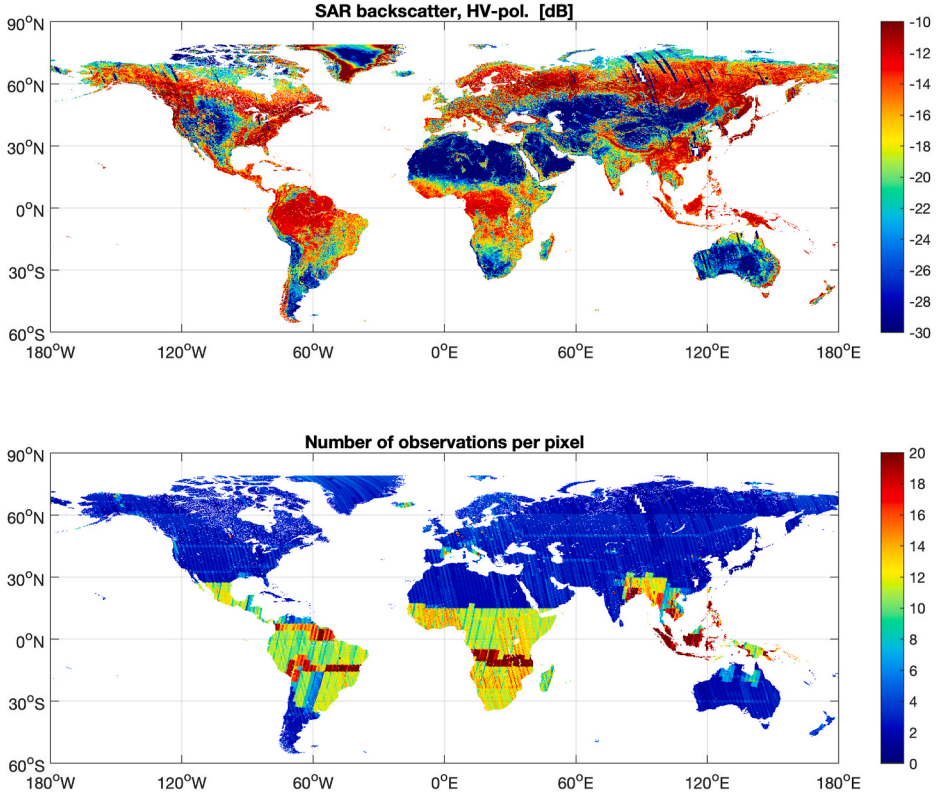

Fig. 1. Average per-pixel values of combined ALOS-2 FB and WB HV-polarized backscatter observations for 2020 (top panel) and corresponding number of observations (bottom panel).

(iv) an image of the date of acquisition of the image and (v) a mask indicating whether a pixel is located over land or (ocean) water, as well as pixels affected by radar shadow and layover. Each layer was spatially averaged to a pixel size of 100 m and inserted into the 1° gridding system. Cross-correlation of the WB data with respect to the FB dataset indicated sub-pixel co-registration accuracy.

2.1.2. Sentinel-1

The Sentinel-1 mission consists of two identical C-band (wavelength: 6 cm) SAR satellite units (1A and 1B) which began operating together in 2017, although Sentinel-1A started operation in late 2014. Each unit has a 12-day repeat-pass interval, but their combination gave images every six days when they were both operational. Sentinel-1A is still operating, but Sentinel-1B failed at the end of 2021. Over land, Sentinel-1 mostly operates in the Interferometric Wide Swath (IWS) mode, acquiring data in dual-polarization (HH + HV or VV + VH) with a spatial resolution of approximately 20 m in range and 5 m in azimuth, and covering a swath of approximately 250 km. For the polar regions, with some limited extension over northern regions, Sentinel-1 operates in Extended Wide Swath (EWS) dual-polarization mode, covering a swath of more than 400 km with a spatial resolution of 40 m in range and 20 m in azimuth. The EWS mode is not just a complement to IWS but is an independent mode defined to give frequent coverage at moderate resolution.

The increasing orbital overlap of IWS acquisitions towards the poles yields an increasing number of observations within a repeat-pass cycle of 12 days for a given point on the ground. For regions observed with both units along both ascending and descending paths, one or more observations per day are possible. In contrast, the large overlap of adjacent orbital tracks in EWS mode provides a very high number of observations within the repeat-pass cycle of each unit, so that several observations each day are possible at the highest latitudes.

The annual wall-to-wall mapping capability of Sentinel-1 is demonstrated by the number of observations available in 2020 (Fig. 2); latitudes outside 75°N and 56°S are not shown as they are irrelevant for AGB. We considered all IWS images acquired by both units except over Europe, where we discarded the images acquired by the 1B unit because they were redundant; the highest observation density was still over Europe (Fig. 2). Global coverage was achieved for all forests except in small regions in northern Canada and Siberia. Outside Europe, hazard-prone areas were imaged more frequently than other areas. As a minimum, dual-polarized observations every 12 days were available, resulting in approximately 60 observations per pixel with two units. Before 2017, the density of observations was lower, with occasional gaps in regions with low observational priority (e.g., northern latitudes and deserts), in which case some gap-filling was possible with EWS data. As with ALOS-2, the VH-polarized backscatter exhibits sensitivity to forest cover and density (Fig. 2), but with weaker contrast between high and low biomass forest, such as between rainforest and savannas in South America and Africa. As for ALOS-2, banding occasionally affected the imagery due to imperfect calibration across Sentinel-1 swaths and the scatterer-specific effect of local incidence angle on the backscatter.

Pre-processing (Fig. S2) started from ground-range projected images of SAR backscatter intensity. Calibration and noise reduction used the calibration gain and the noise factors reported in the image metadata. Precise orbit information was used to replace state vectors provided in the metadata. Boxcar averaging of the backscatter in a 15 × 15 window provided a Multi-Look Intensity (MLI) image with pixels of size 150 m in both range and azimuth. This size was selected for consistency with the dataset of Environmental Satellite (Envisat) Advanced SAR (ASAR) backscatter images (Santoro et al., 2015) covering 2005–2012, and thus support studies based on multi-decadal records of C-band observations.

Each MLI image was terrain-geocoded to the map geometry of the DEM. We used the same procedure as for the ALOS-2 PALSAR-2 imagery in which a look-up table related the geometry of the Sentinel-1 image and the map geometry. In addition, images of local incidence angle, pixel area and terrain slope and aspect angles were generated. Pixels

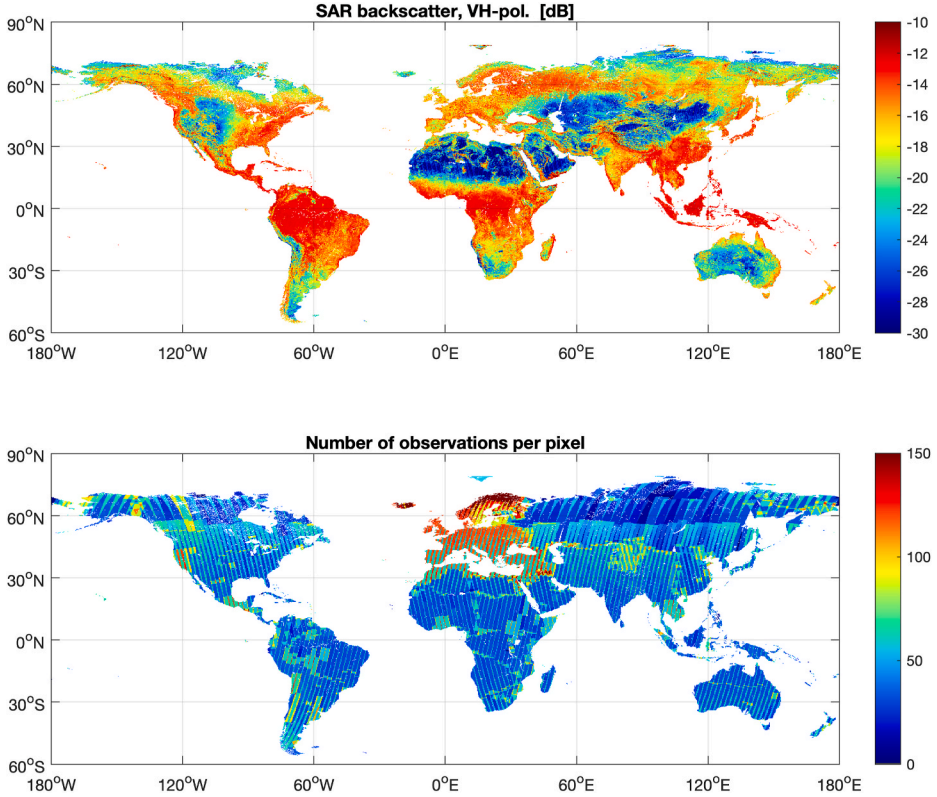

Fig. 2. Average per-pixel values of Sentinel-1 VH-polarized backscatter observations for 2020 and corresponding number of observations. The image with the number of observations per pixel is constrained between 0 and 150 to enhance the contrast outside Europe.

affected by radar layover or shadow were flagged in a binary mask. Since precise orbits were used, there was no need to refine the geocoding look-up table. The co-registration error between the reference DEM and the Sentinel-1 imagery was below 1/10th of the output pixel size (i.e., less than 15 m). To compensate for distortions of the SAR backscatter due to sloping terrain, the normalization factor for true pixel area was applied to each Sentinel-1 image. In addition, the σ^0 measurement was converted to γ^0. Finally, each MLI backscatter image normalized for pixel area was terrain geocoded with the geocoding look-up table and tiled to the pre-defined 1° × 1° grid.

Because the temporal correlation between individual backscatter observations was high, especially over short periods of time (Fig. S3), the Sentinel-1 dataset was reduced to monthly averages of SAR backscatter for each polarization. Shorter time scales would have only marginally reduced the amount of data because of the 12-day interval between image acquisitions. Longer time scales would have reduced the seasonal backscatter signal, which allows better retrieval accuracy than retrieval based on a single image (Santoro et al., 2011).

2.1.3. Precision of the SAR backscatter measurements

The precision of a backscatter measurement is affected by the radiometric and calibration accuracies, thermal noise and speckle. SAR pre-processing introduces additional uncertainty related to: (i) the precision of the geocoding transformation and resampling between radar and map geometries, (ii) the horizontal and vertical precision of the DEM used as reference for the map geometry, and (iii) the precision of the pixel area and local incidence angle used to normalize the backscatter for slope-induced effects on the backscatter. Since the pixel-level uncertainties in the DEMs were unavailable, we could not estimate the variance of a backscatter measurement from the individual variances of the terms listed above. The variance was estimated empirically by equating it to the Equivalent Number of Looks (ENL) (Oliver and Quegan, 1998) in Eq. (1), where μ represents the expected value of the SAR backscatter and σ its standard deviation.

$$ENL = \frac{\mu^2}{\sigma^2} \quad (1)$$

The ENL was estimated for each 1° × 1° grid cell and for each SAR image from the mean and standard deviation of SAR backscatter measurements with at least 95% canopy density based on the MODIS Vegetation Continuous Fields dataset (DiMiceli et al., 2011). This approach was adopted as surfaces with very dense canopy were assumed to represent the most homogeneous type of land surface. The ENL estimates spread over a wide range of values (Fig. 3), due to scattering inhomogeneities and a variable number of observations per grid cell. For Sentinel-1, the median values of the ENL were 124 and 136 for the VV- and VH-polarization respectively, while for PALSAR-2 they were equal to 50 (FB mode) and 19 (WB mode), regardless of the polarization. The larger values for Sentinel-1A come from the higher level of aggregation. More rigorous analysis that estimated ENL in polygons manually drawn to encompass targets with homogeneous backscatter resulted in slightly higher values (~150 for Sentinel-1 and >80 for ALOS-2). For simplicity, we used these latter estimates as single, global ENLs characterizing the precision of the SAR backscatter observations. ENLs of 150 and 80 correspond to a standard deviation of 0.34 dB and 0.46 dB for Sentinel-1 and ALOS-2, respectively.

2.2. LiDAR-based metrics of forest structure

2.2.1. ICESat GLAS

Between 2003 and 2009, the Geoscience Laser Altimeter System (GLAS) on board ICESat collected information about the vertical structure of forests in ca. 65 m diameter footprints collected every 170 m along track. The distance between tracks was of the order of tens of km and increased towards the Equator. From the GLA14 product (version

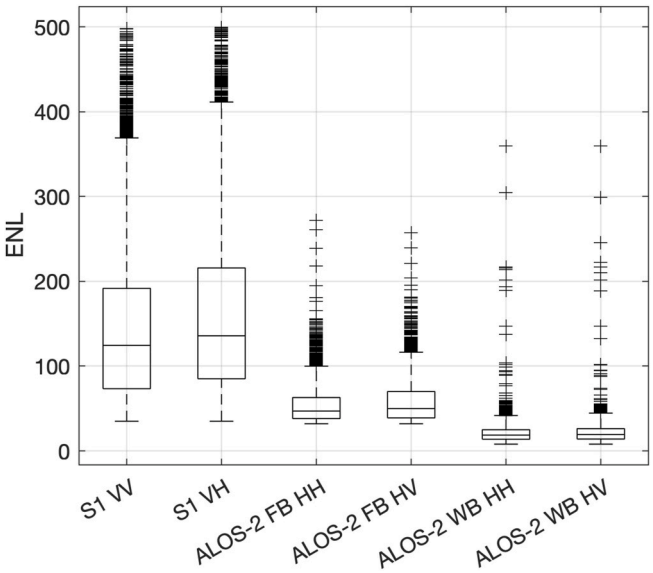

Fig. 3. Box plots representing the distribution of the ENL estimates from 1° × 1° grid cell per SAR sensor, mode and polarization. Each box shows the median value (central mark), the interquartile range (edges of the box), the most extreme data points not considered outliers (whiskers) and the outliers, defined as data points more than three standard deviations away from the median (plus markers).

34) (https://nsidc.org/data/gla14/versions/34), which provides altimetry data for land surfaces only to which geodetic, instrument and atmospheric corrections had already been applied, the raw waveform was modeled with a multi-mode Gaussian (Hofton et al., 2000). The GLAS data were used to estimate canopy density (*CD*), defined as the ratio of energy received from the canopy (returns above the ground peak) to the total energy received, and the canopy height (*h*), defined as the distance between the ground peak and signal start. This is referred to as relative height 100 (*RH100*), i.e., the 100th percentile of waveform energy relative to ground elevation. Pre-processing and filtering (Los et al., 2012; Simard et al., 2011) resulted in a database of 26.5 million valid footprints (Santoro et al., 2022). Because of the large distance between the orbital tracks and the strong filtering applied to the GLA14 dataset, the coverage was not uniform, with large gaps in South China and the southernmost regions of South America, Africa and Australia (Santoro et al., 2022) (Fig. S4). For the standard deviation (SD), we assumed a value of 20% of the individual estimates of CD and RH100 (Neuenschwander et al., 2008).

2.2.2. ICESat-2 ATLAS

Unlike the GLAS sensor, the Advanced Topographic Laser Altimeter System (ATLAS) onboard the ICESat-2 satellite uses photon counting to retrieve elevation (Neuenschwander and Pitts, 2019). ATLAS splits the laser into six beams arranged as three pairs of beams approximately 3.3 km apart (Markus et al., 2017). Each pair consists of a strong and weak energy beam (4:1 ratio). The ICESat-2 ATL08 product contains geophysical parameters related to vegetation and terrain heights (Neuenschwander and Pitts, 2019). The parameters are provided in the form of data segments with a 100 m step size along the flight direction. According to the data producer, the 98th percentile of all height values within a segment (RH98) is most suitable to represent the canopy height. A metric representative of canopy density is not provided because the full waveform is not available. From the original photon data, the original files were reformatted into segments of 100 m length and 25 m width (https://github.com/remotesensinginfo/pysl4land).

ICESat-2 files covering the years 2019–2021 were used, resulting in filtering 334 million segments of data. Based on Neuenschwander and Pitts (2019), we discarded segments that were: (i) acquired by the weak

beams because of the very small number of photons recorded from the forest floor, in particular in dense canopies, (ii) characterized by less than three photons reflected by the canopy, (iii) flagged as not belonging to natural vegetation in the metadata and (iv) exhibited an elevation differing more than 25 m from the reference DEM used in all ATL products. In addition, values greater than 50 m were filtered out because they frequently occurred in sparsely vegetated or unvegetated regions.

Fig. 4 shows maps of average canopy height, the corresponding average of height SD and the number of segments for a grid cell spacing of 0.1° (panels (a), (g) and (h), respectively). Adopting a 0.1° cell size and using data from three years, we could characterize the spatial distribution of canopy height globally with high precision and only minor gaps in regions that are poorly vegetated. The spatial patterns of the average canopy height map correspond to the distribution of forest height obtained with ICESat GLAS, although the coverage by the latter was poorer (Fig. S4). The ICESat-2 mean canopy heights agree strongly with the corresponding ICESat values (panel (c)), albeit for heights above 30 m where the ICESat-2 values tend to be larger. The differences between the two datasets when ICESat-2 canopy height exceeds 40 m are due to obviously erroneous values that were undetected during filtering.

Fig. 4 also shows the 90th and the 98th percentile of segment-level canopy heights for each 0.1° grid cell. These two layers quantify two terms in the AGB retrieval model, i.e., the height of dense forests (h_{df} in Section 3.2) and the maximum canopy height ($h_{\max}$ in Section 3.1). The maximum and mean canopy height are highly correlated (panel (f)) and their difference decreases for taller forests.

2.3. Auxiliary raster datasets

The tree canopy and bare ground cover datasets were derived from Landsat 7 ETM + imagery acquired around 2010 and have a pixel size of approximately 30 m (Fig. S5) (Hansen et al., 2013). Both quantities are provided as values between 0 and 100% per pixel. Changes of tree cover between 2010 and 2020 are not accounted for because the maps of losses (annual) and gains (single value) published alongside the percentage tree cover map do not report the magnitude of the change. It was assumed that such changes did not impact the estimation of the retrieval model parameters.

The CCI Land Cover dataset stratifies land cover into 22 classes and consists of global annual datasets between 1992 and 2020 with a spatial resolution of 300 m (Defourny et al., 2017). The datasets coincident with the SAR images were used in the model training process to exclude SAR observations not associated with natural vegetation since these could bias the retrieval model parameters (Santoro et al., 2015).

The Copernicus GLO-30 DEM data product had a pixel size of 1 arc-second, i.e., approximately 30 m at the Equator, with World Geodetic System 1984 (WGS84) and Earth Gravitational Model 2008 (EGM2008) horizontal and vertical reference, respectively. The absolute vertical and horizontal accuracy of the DEM has been reported to be better than 4 m and 6 m, respectively (Fahrland, 2022). To adhere to the target pixel size of the SAR data, the DEM was either averaged to 90 m and resampled to 100 m (ALOS-2) or averaged to 150 m (Sentinel-1).

The Terrestrial Ecoregions of the World (TEOW) dataset (Olson et al., 2001) divides the Earth's land surfaces into 825 ecoregions, which are categorized within 14 biomes and eight biogeographic realms. The boundaries of each ecoregion, biome and realm correspond to the original extent of natural communities prior to major land-use change. The dataset was rasterized and reprojected to the geometry of each of the SAR datasets. It was used to segment the ICESat GLAS dataset when estimating the model coefficient relating canopy density and canopy height measurements from the individual waveforms.

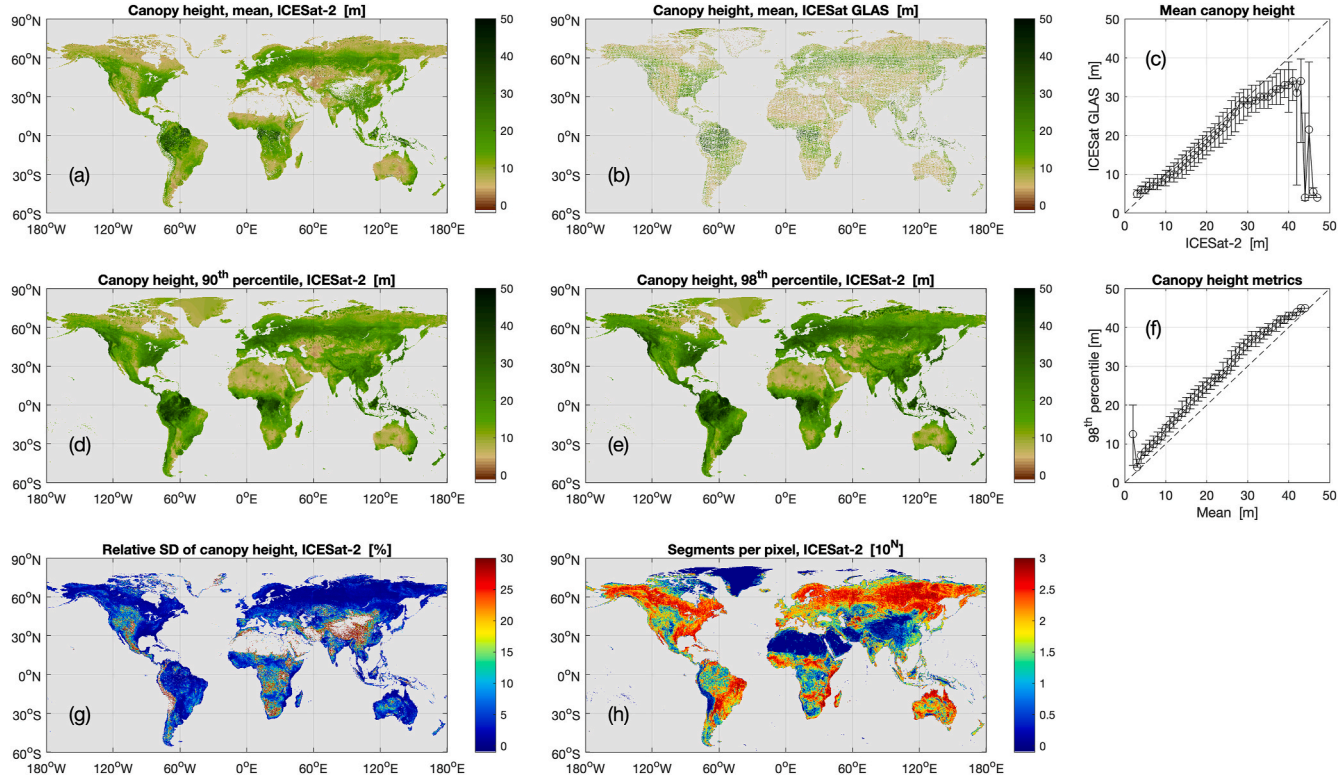

Fig. 4. Global distribution of canopy height metrics computed at 0.1° spatial scale (a) mean ICESat-2 (b) mean ICESat, (d) 90th percentile ICESat-2, (e) 98th percentile ICESat-2, (g) average standard deviation and (h) number of segments. The ICESat-2 values were based on segment-level observations taken between 2019 and 2021. In panel (d) and (e), data gaps were filtered by inpainting over neighboring valid values. Panel (c) shows the median (circles) and interquartile range (vertical bars) of mean canopy height from the ICESat GLAS dataset corresponding to a given height integer in the ICESat-2 dataset. Panel (f) shows the median (circles) and interquartile range (vertical bars) of the 98th percentile of canopy height corresponding to a given mean canopy height level in the ICESat-2 dataset.

2.4. AGB from field inventory

2.4.1. Plot inventory measurements

The plot data originated from National Forest Inventories (NFI) and research networks, thus embodying different statistical sampling strategies and functions predicting AGB from the field measurements. After screening and temporal harmonization of the AGB values (Araza et al., 2022), the database of plot measurements consisted of 59,052 AGB values representative of the year 2020. The database is opportunistic in nature, so the spatial distribution of the samples is uneven and several regions of the world are not represented (Fig. S6).

Plot-based AGB values have errors which decrease with the size of the plot (Réjou-Méchain et al., 2019), so the data in our analysis were split into three Tiers. Data from plots $\leq$0.6 ha (minimum size: 0.015 ha), which are typically collected by NFIs, were in Tier 1. This category was the most populated with 58,716 samples. Tier 2 consisted of plots with areas in the range 0.9–3 ha and included 315 samples. Large plots ($\geq$6 ha) belonged to Tier 3, which consisted of 21 samples. Since the plots in Tier 1 were unlikely to be fully representative of the AGB in the 1-ha area of a pixel and comparison of plot- and map-based AGB only becomes meaningful when averaging over multiple values (Araza et al., 2022), we considered Tier 1 data only when at least five plots were located in a $0.1^\circ \times 0.1^\circ$ grid cells, with the mean of all plots in the grid cell used as the AGB value, as originally proposed in Santoro et al. (2021a).

2.4.2. Sub-national average values

Sub-national statistics on AGB were gathered for 106 countries. A small fraction of them were computed directly for countries that provided access to the original plot data collected as part of their NFI surveys. However, most were instead gathered from reports and table statistics published by the NFIs. Such NFI-based values were available except for large parts of Africa, the Middle East, parts of Southeast Asia and the Caribbean (Fig. S7). For 94 of the countries without NFI data, national averages of AGB are reported in the FAO Forest Resources Assessment (FRA) for 2020 (FAO, 2020). The 50 remaining countries without NFI-based statistics or AGB reported in the FRA 2020 database were either very small, e.g., in the Caribbean or Oceania, or had little forest cover. Our database of AGB averages consisted of 761 values for sub-national administrative or ecological units and 94 values at national level taken from the FRA (Annex 1, Supplement).

3. Methods

The flowchart in Fig. 5 shows the interdependencies of datasets and models in the CCI Biomass retrieval algorithm. The retrieval was based on the BIOMASAR approach, which estimates a forest variable related to the biomass density of woody vegetation (AGB or growing stock volume, GSV) from a dense time series of SAR backscatter observations (Santoro et al., 2011, 2015, 2021a). Here, multi-temporal Sentinel-1 C-band backscatter data were used to generate a set of global estimates of AGB with a pixel size of 150 m using the BIOMASAR-C algorithm; these were then resampled to 100 m to match the AGB estimates obtained from multi-temporal L-band backscatter data using the BIOMASAR-L algorithm. Auxiliary datasets (Section 2.3), but not *in situ* measurements, were used to calibrate the parametric models embedded in the BIOMASAR algorithms. To reduce possible systematic errors in the BIOMASAR-L and BIOMASAR-C estimates, these datasets were merged. This procedure is implemented for data acquired within one year. With several years of EO data available, the resulting estimates of AGB were refined by minimizing their error with a cost function. The precision of the estimates was estimated at each step and for the final AGB values at each 100 m pixel. Also indicated in the shaded part of Fig. 5 are possible routes to improvement of the retrieval by linking it with datasets or methods superior to those used in this paper.

3.1. The BIOMASAR algorithm

The theoretical basis of the BIOMASAR algorithm has been extensively presented in previous studies (Cartus et al., 2012; Santoro et al., 2011). While retaining the same structure, empirical coefficients have been replaced with functions trained on spaceborne LiDAR observations and AGB values derived from measurements by national forest inventories (Fig. 6).

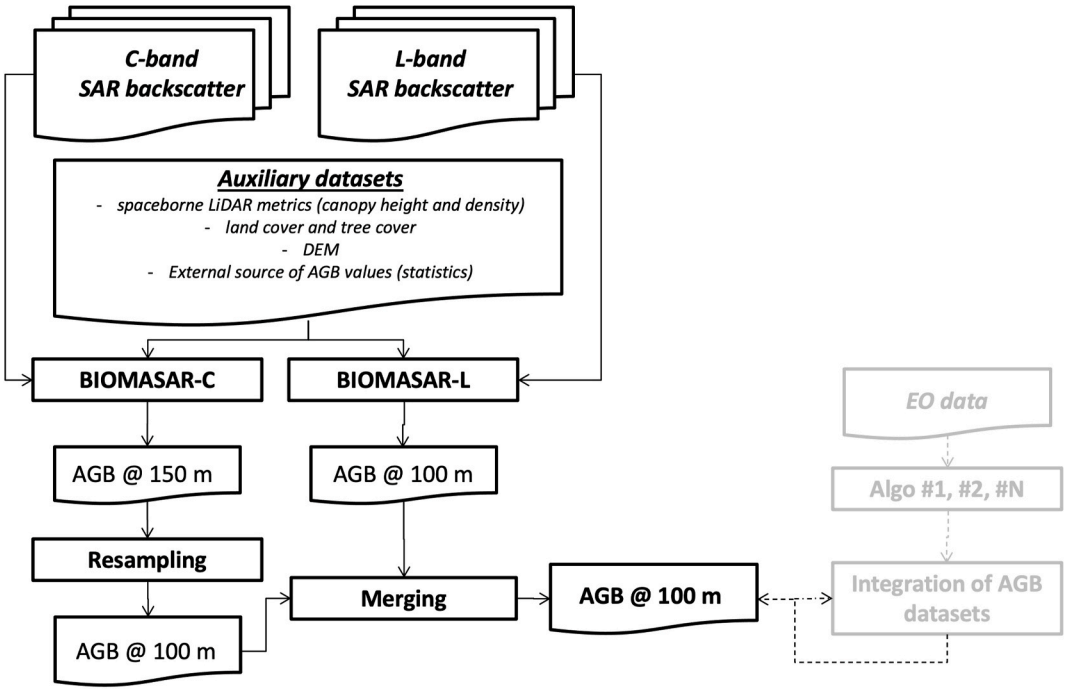

Fig. 5. Functional dependencies of datasets and approaches forming the CCI Biomass global biomass retrieval algorithm. The shaded part of the flowchart represents potential improvements resulting from the implementation of supplementary retrieval techniques.

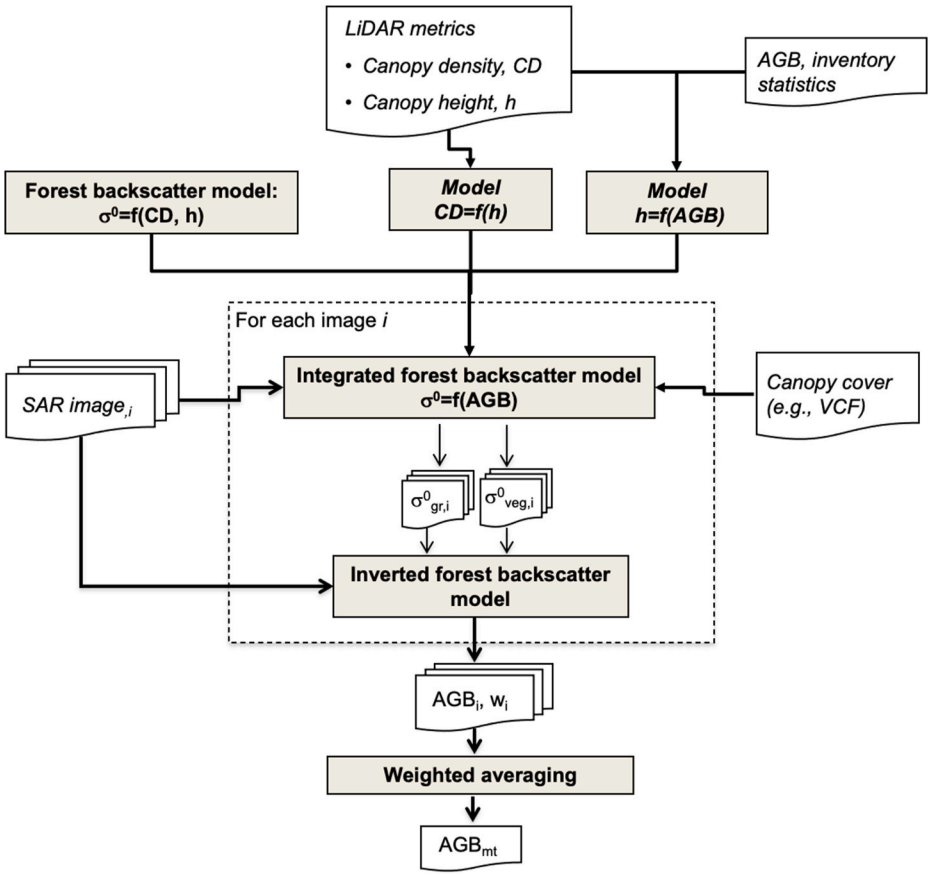

Fig. 6. Flowchart of the BIOMASAR algorithm.

BIOMASAR-C and -L both exploit the Water Cloud Model in Eq. (2) (Askne et al., 1997) to estimate AGB from SAR backscatter. This model relates the backscatter from a forest to horizontal and vertical properties of the scattering medium, accounting for gaps in the canopy and for attenuation of the signal along the two-way path inside the canopy. The effect of canopy gaps is quantified by means of two terms that include the area-fill factor, η, which is approximated by the canopy density (CD), i.e., $\eta = CD$. The attenuation within the forest canopy was characterized by its two-way transmissivity, modeled as an exponential function of canopy height, h, with transmissivity coefficient, α. The total backscatter from a forest is then represented as a sum of contributions from the ground, σ^0_{gr}, and the vegetation layer, σ^0_{veg}:

$$\sigma^0_{for} = (1-\eta)\sigma^0_{gr} + \eta\sigma^0_{gr}e^{-\alpha h} + \eta\sigma^0_{veg}\left(1-e^{-\alpha h}\right) \quad (2)$$

To express the Water Cloud Model as a function of AGB, it was integrated with two models relating the two structural variables, η and h, to AGB (Santoro et al., 2021b, 2022). Eq. (3) relates canopy density and canopy height by means of an exponential function with the empirical coefficient q:

$$\eta = 1 - e^{-qh} \quad (3)$$

Eq. (4) relates canopy height and AGB, based on a power-law function with coefficient p_1 and p_2, as proposed in the literature (Asner and Mascaro, 2014; Coomes et al., 2017; Dalponte et al., 2019; Labriere et al., 2018):

$$AGB = p_1 h^{p_2} \quad (4)$$

Inverting Eq. (4) to obtain $h = (b_1 \bullet AGB)^{b_2}$, with $b_1 = 1/p_1$ and $b_2 = 1/p_2$, and substituting into Eqs. (3) and (2) leads to the integrated retrieval model in Eq. (5), where the forest backscatter is expressed as a function of AGB only:

$$\sigma^0_{for} = \left[1-\left(1-e^{-q\bullet(b_1\bullet AGB)^{b_2}}\right)\left(1-e^{-\alpha\bullet(b_1\bullet AGB)^{b_2}}\right)\right]\sigma^0_{gr} + \left(1-e^{-q\bullet(b_1\bullet AGB)^{b_2}}\right)\left(1-e^{-\alpha\bullet(b_1\bullet AGB)^{b_2}}\right)\sigma^0_{veg} \quad (5)$$

Estimation of the unknown model parameters for forest structure (q, p_1 and p_2) and backscatter (σ^0_{gr}, σ^0_{veg} and α) for each backscatter image is described in Section 3.2. Eq. (5) is then inverted to express AGB as a function of the measured backscatter (Fig. 6). However, saturation of Eq. (5) imposes a constraint on the maximum retrievable AGB. This is defined as the AGB estimated with Eq. (4) for maximum height, $h_{\max}$ (Section 2.2):

$$AGB_{max} = p_1 (h_{max})^{p_2} \, . \quad (6)$$

AGB estimates corresponding to backscatter values outside the range 0 to AGB_{max} Mg ha^{-1} were replaced with either 0 or AGB_{max}, whichever was closer.

If N observations of SAR backscatter (and hence estimates of AGB) are available over a period when AGB is unlikely to have changed significantly (e.g., one year), an estimate of AGB with reduced variance, AGB_{mt} (Eq. (7)), can be obtained by weighted averaging of the N individual AGB estimates (Kurvonen et al., 1999; Santoro et al., 2011):

$$AGB_{mt} = \frac{\sum_{i=1}^{N} w_i AGB_i}{\sum_{i=1}^{N} w_i} \quad (7)$$

The weights, w_i, are defined as the vegetation-to-ground backscatter difference in dB, σ^0_{veg} - σ^0_{gr}, normalized by the maximum backscatter difference across the multi-temporal stack of observations (Santoro et al., 2011):

$$w_i = \frac{\sigma^0_{veg,i} - \sigma^0_{gr,i}}{max\left(\sigma^0_{veg,i} - \sigma^0_{gr,i}\right)} \quad (8)$$

3.2. Estimation of the model parameters

For the structural model in Eq. (3), canopy density and canopy height from spaceborne LiDAR data allowed global estimation of the coefficient q (Kay et al., 2021; Santoro et al., 2022). Since global canopy density metrics are lacking from the more recent spaceborne LiDAR missions, an already available set of estimates of q based on ICESat GLAS metrics were used here (Kay et al., 2021). This dataset (Fig. S8) was obtained by fitting Eq. (3) in each of the 827 strata of the World Wildlife Fund terrestrial ecoregion dataset (Olson et al., 2001). The estimation was then refined in ecoregions covering an area larger than 1° × 1° where the model fit was undertaken at the scale of 1°-wide grid cells.

Spaceborne LiDAR data are also used to train the structural model in Eq. (4). However, lack of a spatially explicit dataset of AGB measurements with spatial resolution comparable in size to the LiDAR footprints implies that estimation of the coefficients in Eq. (4) must rely on other AGB measurements. The relationship between AGB and canopy height was initially characterized globally with the ICESat GLAS dataset for canopy height and map-based values of AGB, both averaged to 0.25° (Santoro et al., 2022). This allowed the two model parameters, p_1 and p_2, in Eq. (4) to be estimated at any location, but biases in the AGB estimates affected the estimation. To mitigate this, the map-based values are replaced by the AGB averages from inventory measurements at the level of administrative or ecological units. These are expected to have significantly smaller bias, but at the expense of spatial detail. To estimate p_1 and p_2, these AGB averages are regressed to corresponding average values of canopy height from the ICESat-2 dataset. Spatial characterization of the height-to-AGB function was achieved by stratifying the data by continent and major ecological traits (Fig. S9). The definition of the 17 strata followed an additional set of criteria based on number of data values, availability of NFI-based values and uniform representation of the range of AGB. Such a stratification could not capture small-scale variability of the height-to-AGB relationship but establishes reliable predictions of AGB that are consistent with macro-ecological patterns. It also minimizes the risk of large regions being characterized by AGB biases attributed to an imperfect function.

The coefficients σ^0_{gr} and σ^0_{veg} respectively represent the backscatter intensity from a theoretically unvegetated surface and a canopy dense enough to prevent any return from the soil. Both are idealizations, approximated using the average backscatter from unvegetated surfaces (so-called "ground" pixels) and dense forest canopies ("dense forest" pixels) within a window (Santoro et al., 2011). The estimation window corresponds to the size of a tile, i.e., 1° × 1°, in which it is assumed that there are sufficient "ground" and "dense forest" pixels to reliably estimate σ^0_{gr} and σ^0_{veg}. To avoid distorting the estimate of σ^0_{gr}, areas with very low canopy density not corresponding to natural vegetation (cropland, urban areas, bare soil, permanent snow and ice and water bodies) are masked out using the CCI Land Cover dataset.

To account for the dependence of SAR backscatter on local incidence angle, the C- and L-band forest backscatter models are trained separately with tree cover values for five 10° wide intervals of local incidence angle, starting with 20° and ending with 70°. Areas affected by layover and shadow are masked out.

While the average backscatter for an unvegetated surface is a reasonable approximation for the coefficient σ^0_{gr}, obtaining the average backscatter for dense forest canopies requires compensating for ground backscatter from gaps in the canopy (Santoro et al., 2011):

$$\sigma^0_{veg} = \frac{\sigma^0_{df} - \left(1 - \eta_{df} + \eta_{df} e^{-\alpha_{df}}\right)\sigma^0_{gr}}{\eta_{df}\left(1 - e^{-\alpha_{df}}\right)} \quad (9)$$

Eq. (9) was derived by inverting Eq. (2) for σ^0_{veg} and equating all the forest-related coefficients to those appropriate for dense forests, $\sigma^0_{for} = \sigma^0_{df}$. The parameters η_{df} and h_{df} represent the average canopy density and height for dense forests, respectively. To reduce the number of variables in Eq. (9), η_{df} was replaced by its model-based value from Eq. (3) with $h = h_{df}$.

Valid estimation of σ^0_{gr} and σ^0_{df} requires search windows with enough pixels belonging to each category, otherwise they will be undetermined. This can be avoided by expressing the forest backscatter (Eq. (2)) as a function of canopy density only, using Eq. (3), and regressing between backscatter and canopy density, thus also allowing α to be estimated:

$$\sigma^0_{for} = (1-\eta)\sigma^0_{gr} + \eta\sigma^0_{gr} e^{\alpha \frac{\log(1-\eta)}{q}} + \eta\sigma^0_{veg}\left(1 - e^{\alpha \frac{\log(1-\eta)}{q}}\right) \quad (10)$$

This transformation is performed because, although global datasets of canopy height (Lang et al., 2022; Potapov et al., 2021; Simard et al., 2011) and tree cover density (DiMiceli et al., 2011; Hansen et al., 2013) are both available, the latter are likely to be more reliable because of the physical properties of the optical data from which they are both derived.

3.3. Merging of AGB estimates

The estimates of AGB from the C- and L-band SAR datasets from Eq. (7) have distinct uncertainties due to different decreases in sensitivity of backscatter to increasing AGB, the number of SAR observations, and the quality of the SAR pre-processing. To merge them into a single value, we adopted a further weighting scheme in which the estimate of AGB for a given year y is obtained as:

$$AGB_{merged,y} = AGB^C_{mt,y} + w_{M,y}\left(AGB^L_{mt,y} - AGB^C_{mt,y}\right) \quad (11)$$

In Eq. (11), $AGB^C_{mt,y}$ and $AGB^L_{mt,y}$ represent the estimates of AGB from the C-band and the L-band SAR datasets for a given year y obtained with Eq. (7). The weight $w_{M,y}$ was designed to account for the sensitivity of AGB to backscatter for C- and L-band represented by the model-based transmissivity term and the number of SAR observations:

$$w_{M,y} = \left|\frac{\partial T_L}{\partial AGB}\sqrt{N_{L,y}}\right| - \left|\frac{\partial T_C}{\partial AGB}\sqrt{N_{C,y}}\right| \quad (12)$$

In Eq. (12) the suffices L and C on T and N indicate the frequency band and the number of observations of the SAR dataset used in the retrieval. To compute the derivative in Eq. (11), the transmissivity term is expressed as a function of AGB through Eqs. (3) and (4):

$$T(AGB) = 1 - \eta(h(AGB)) + \eta(h(AGB)) \bullet T_{tree}(h(AGB)) \quad (13)$$

Since the values obtained with Eq. (12) can be either positive or negative, $w_{M,y}$ in Eq. (11) corresponds to the normalized value from Eq. (12).

$$w_{M,y} = \frac{\left(w_{M,y} - min\left(w_{M,y}\right)\right)}{max\left(w_{M,y} - min\left(w_{M,y}\right)\right)} \quad (14)$$

When the SAR dataset spans several years, better inter-annual agreement of the AGB estimates is obtained by refining each of the values of $w_{M,y}$. For this, $w_{M,y}$ in Eq. (11) is first computed for each year separately and then all $w_{M,y}$ are modified by minimizing the cost function (CF) in Eq. (15):

$$CF = \sum_{y1=Y_0}^{Y_{T-2}} \sum_{y2=y1+1}^{y1+2} \left|AGB_{merged,y1} - AGB_{merged,y2}\right|^2 \quad (15)$$

CF utilizes the AGB estimates obtained from Eq. (11) for pairs of consecutive years ($AGB_{merged,y1}$ and $AGB_{merged,y2}$). In Eq. (15), Y_0 and Y_T represent the first and the last year (i.e., 2015 and 2021). As initial values, the minimization used the values of $w_{M,y}$ from Eq. (13) for each year. The final value for each of the $w_{M,y}$ coefficients between Y_0 and Y_T

was obtained by constraining the search space to ±20% of their initial values. These values are then inserted in Eq. (11) to obtain the final estimate of AGB for each of the years.

Defining weights at the 100 m pixel size of the maps risked strong fluctuations appearing in the weights of adjacent pixels and the generation of artefacts. They are therefore generated at the scale of 0.1° and then resampled with bilinear interpolation to the full resolution.

3.4. Uncertainty model

Accuracy describes how well the estimate of a certain quantity matches its true value. Two global statistical measures of the accuracy of an estimator are commonly used: bias, which is the expected value of the difference between the estimated and true value, and precision, which indicates the variability of the estimates and is usually quantified by the SD. More complete descriptors could include, for example, confidence intervals on the estimates or the full error distribution. The latter descriptors are practically impossible to obtain in our case because the errors of some of the parameters involved in the AGB retrieval scheme could only be assumed. While bias can normally only be quantified if the true value of AGB is known, the precision of an AGB estimator can be quantified using an uncertainty model based on the SDs of the observations and the model parameters.

The SD of an AGB estimator using a single observation of SAR backscatter is quantified by propagating the SDs of: (i) the measured SAR backscatter (Section 2.1.3), (ii) the estimates of the forest backscatter model parameters α, σ^0_{gr} and σ^0_{veg}, (iii) the coefficient of the model relating canopy density and canopy height, q, and (iv) the coefficients of the model relating canopy height and AGB, p_1 and p_2. Each parameter of the retrieval model was perturbed M times based on their individual SDs, and the SD of the AGB estimate was taken to be equal to the SD of the M AGB estimates from Eq. (5). This became stable when M exceeded 100 but was substantially larger for fewer iterations.

The SD of the AGB estimate provided by the linear combination in Eq. (7) consists of a variance component from the appropriately weighted variances of the individual AGB estimates and a covariance component that accounts for the correlation between errors in AGB estimates.:

$$\delta(AGB_{mt})^2 = \sum_{i=1}^{N} w_i^2 \delta(AGB_i)^2 + 2\sum_{i=1}^{N-1}\sum_{j=i+1}^{N} w_i w_j Cov\left(AGB_i, AGB_j\right) \quad (16)$$

In Eq. (16), $\delta(AGB_i)^2$ and $\delta(AGB_{mt})^2$ represent the variance of AGB estimate i and of the weighted average from Eq. (7), respectively. The covariance term is expressed as:

$$Cov\left(AGB_i, AGB_j\right) = \delta AGB_i \delta AGB_j r_{ij} \quad (17)$$

where r_{ij} is the correlation of errors between the estimates of AGB from image observations i and j. Given the lack of extensive and evenly sampled measurements of AGB, the correlation of errors between each pair of AGB estimates from observation i and j is estimated with reference to maps of AGB derived from airborne LiDAR. We used data obtained with the methodology described in Labriere et al. (2018) from sites distributed across the U.S. (https://data.neonscience.org), the Brazilian Amazon (Keller et al., 2019), Kalimantan (Ferraz et al., 2018) and Australia (https://portal.tern.org.au/metadata/TERN/4ff0b4c9-cfa0-4d09-9520-b5402adc583f).

The SD of the AGB estimate from the combination of the BIOMASAR-C and -L AGB estimates is then obtained as:

$$\delta(AGB)^2 = w^2(L)\delta\left(AGB_{mt,L}\right)^2 + w^2(C)\delta\left(AGB_{mt,C}\right)^2 \quad (18)$$

3.5. AGB validation

To assess the reliability of the AGB estimates, we computed: (i) the RMSD between map- and plot-based AGB values relative to the average reference AGB and (ii) the difference between map- and plot-based AGB average values (bias). The RMSD was computed as a weighted mean of the errors, where the weights corresponded to the ratio of the forest area to the total forest area.

4. Results

4.1. Training and verification of the height-to-AGB structural model

Average AGB from NFI data is plotted against average canopy height from ICESat-2 in Fig. 7, together with the corresponding fitted power-law function in Eq. (4) for each of the strata in Fig. S9. The power-law model reproduced the observed trend in strata from countries with well-established NFIs (e.g., in Europe, Russia, or North America), while for other strata the model fit was acceptable even though the association between observations was moderate ($R^2 < 0.7$). To test the reliability of the set of models in Fig. 7, we compared them to local and regional model curves published in the literature (Fig. S10), and predicted AGB from ICESat-2 measurements of canopy height and, after averaging them to 0.1° grid cells, compared them with the aggregated Tier 1 AGB values (Section 2.4). Despite considerable dispersion, the data points in Fig. 8 clustered along the identity line with more than 60% of the variance in the reference data being explained by the predicted values and an overall negligible bias. The positive bias for AGB <50 Mg ha^{-1} occurred over Spain, to which we associated the coefficients for Central and Southern Europe. The scaling coefficient p_1 was likely too high because it was driven by AGB values from Central Europe that were mostly larger than 100 Mg ha^{-1}. The negative bias for AGB >400 Mg ha^{-1} occurred in tropical rainforest regions of South America and Africa, in part because the strong filtering applied to the ICESat-2 data caused many segments containing dense forest to be discarded, thus shifting the overall height distribution towards lower values.

4.2. Training and verification of the forest backscatter model

Differences in the response of the backscatter to canopy density, height and AGB mean that the estimation of the three unknown model coefficients (σ^0_{gr}, σ^0_{veg}, and α) had to be adapted to the SAR frequency. Figs. 9 and 10 show examples of estimates for σ^0_{gr} and σ^0_{veg} from BIOMASAR-C and -L, respectively, in four tiles and stratified by local incidence angle. Landsat-based tree cover and the corresponding backscatter values from Sentinel-1 (Fig. 9) and ALOS-2 PALSAR-2 (Fig. 10) are also displayed.

For C-band, we set α = 2 dB/m following a synthesis of studies dealing with attenuation of C-band microwaves in tree canopies (Askne and Santoro, 2005; Cartus et al., 2019). Although attenuation is expected to decrease to approximately 1 dB/m under very dry or frozen conditions (Santoro et al., 2002), the impact on fitting Eq. (8) to SAR backscatter and tree cover values was negligible.

Santoro et al. (2011) proposed to set σ^0_{gr} equal to the median backscatter value for the "ground" pixels in the estimation window. Because these pixels typically cover a range of different types of conditions (e.g., bare soils, grass, shrubs, young trees), the median value was occasionally above the level expected for a surface with tree cover equal to 0%. We therefore revised the definition of the σ^0_{gr} estimate by computing percentiles of the backscatter distribution for tree cover less than 30%. The first quartile was taken to be representative of a hypothetically unvegetated surface (Fig. 9) and gave more accurate retrieval of AGB than other percentiles (not shown here).

The original approach to estimate σ^0_{veg} relied on “dense forest” pixels, defined as pixels with tree cover exceeding 75% of the maximum value in the estimation window. Since this definition becomes questionable in areas of sparse forest, we here relax the threshold and consider all pixels that are potentially forest, i.e., with a tree cover >30%. However, the original definition, which estimated σ^0_{veg} as the median of all backscatter

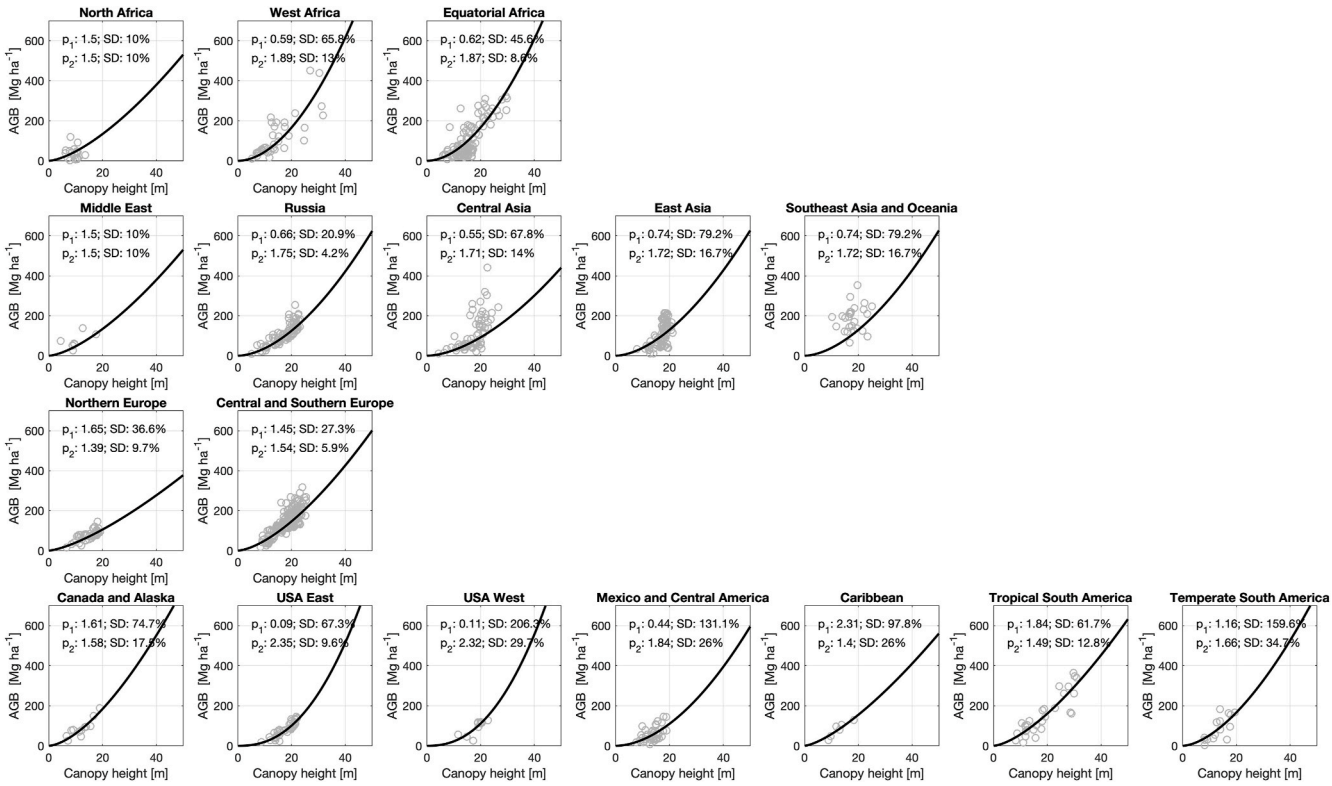

Fig. 7. Observations of average canopy height from ICESat-2 and average AGB at national and sub-national level (circles), and corresponding model fit based on Eq. (4) for the 17 strata in Fig. S9. The 17 panels are here arranged by continent. Each panel reports the estimate of the model's coefficients and their SDs. The model fitted to the observations (solid curve) is extended up to 50 m (dashed curve) in accordance with the canopy height range shown in Fig. 4.

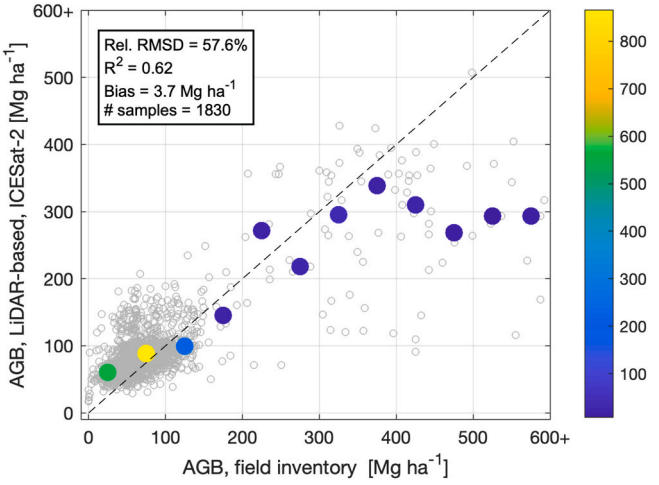

Fig. 8. Comparison of grid cell average values of AGB from field inventory data and from Eq. (4) applied to ICESat-2 canopy height measurements (circles). The filled circles represent the median value of AGB from the LiDAR-based predictions in the corresponding 50 Mg ha^{-1} wide bin of AGB from the inventory-based values. The color bar refers to the number of 0.1° grid cell observations in each AGB bin. (For interpretation of the references to color in this figure legend, the reader is referred to the Web version of this article.)

values for dense forests, caused under-estimates of σ^0_{veg}. To correct this, we obtained a first estimate of σ^0_{veg} by least squares regression of Eq. (10) with σ^0_{gr} and α set as above (red circles in Fig. 9). Since this represents an average backscatter for the densest canopies, it was then compensated using Eq. (9) to obtain σ^0_{veg} (black asterisk at tree cover of 100% in Fig. 9).

For L-band, σ^0_{gr} and α were first estimated from regressing Eq. (10) using pairs of observations of tree cover and backscatter. The regression was constrained with σ^0_{df} (Santoro et al., 2021a) and with $0.2 \leq \alpha \leq 1.5$ dB/m to avoid unrealistic model fits. Eq. (9) was then applied to estimate σ^0_{veg} by compensating σ^0_{df} with the residual ground contribution based on σ^0_{gr}. The estimates of σ^0_{gr} and σ^0_{veg} were then refined using a second regression onto the observations of tree cover and backscatter.

Overall, the estimates of σ^0_{gr} and σ^0_{veg} were reasonable at both frequencies (Figs. 9 and 10). In the area with steep topography (tile N46E011), the relationships between backscatter and canopy density, and therefore the estimates of σ^0_{gr} and σ^0_{veg}, differed significantly depending on the local incidence angle. The compensation of σ^0_{df} to obtain σ^0_{veg} was small; nonetheless, it avoided over-prediction of AGB since even a change of a fraction of a dB has a substantial impact when the observations have weak sensitivity to the variable of interest (Santoro et al., 2021a).

The estimates of σ^0_{gr} and σ^0_{veg} per incidence angle bin followed regular patterns for both C- and L-band (Figs. 9 and 10) which were fitted on a tile-by-tile basis using quadratic functions. These models were then applied to give spatially explicit estimates for each of the two parameters given the local incidence angle for a given SAR backscatter image (Fig. S11).

4.3. Estimation of AGB

The rather simple formulation of the forest backscatter model in Eq. (5) and of the weighting rules in Eq. (7) paired with the weak sensitivity of backscatter to AGB tend to introduce biases in the estimate of AGB from a given sensor. Plots such as those in Fig. 11, where the histogram of AGB from each SAR image in a tile is compared to the histogram of AGB from the multi-temporal combination, can identify sources of errors. For the left-hand panel of Fig. 11, the AGB for most of the pixels was obtained from inverting the backscatter model, with only a few pixels being assigned the maximum AGB. The multi-temporal

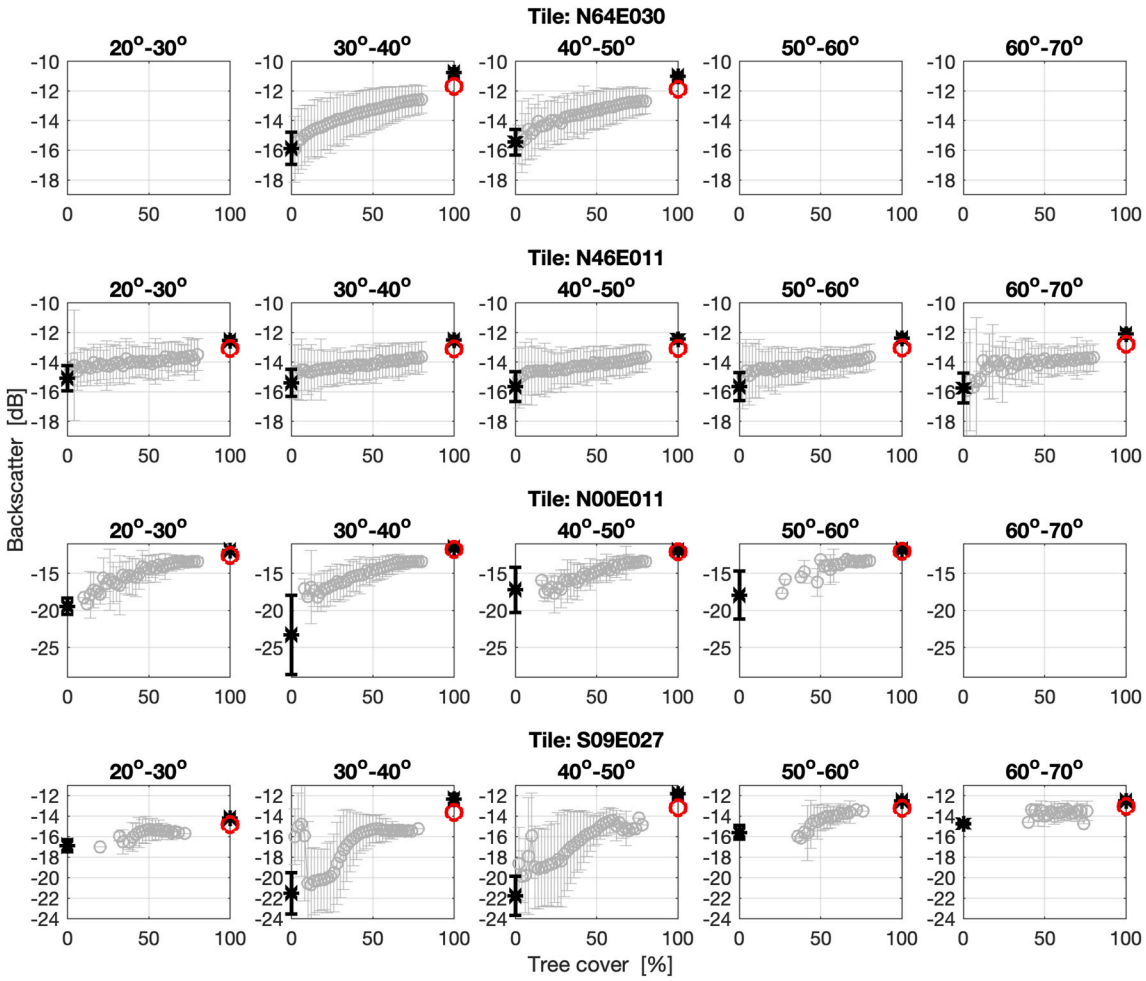

Fig. 9. Observations of tree cover density and Sentinel-1 backscatter stratified by tile (rows) and by incidence angle range (columns). Grey circles and vertical bars represent the median value and the range of values per 2%-wide tree cover bins. The asterisks at tree cover 0% and 100% together with their vertical bars in black represent the estimates of σ^0_{gr} and σ^0_{veg}, respectively, and their SD for the given tile and incidence angle range. Red circles represent the initial estimate of σ^0_{veg} from the regression of Eq. (10). The SAR backscatter data consist of Sentinel-1, VH-polarization observations acquired during July 2020. Blank panels refer to cases not represented in the datasets. (For interpretation of the references to color in this figure legend, the reader is referred to the Web version of this article.)

combination preserved this structure. For the middle panel in Fig. 11, the shape of the histograms varied, and several images were characterized by AGB estimates equal to the maximum AGB, with this being a sign that the backscatter model did not always reproduce the level of the backscatter observations. As a result, the weighted average of the single-image AGBs propagated such biases and its histogram peaks between the histograms of the single-image retrievals and the maximum AGB. The right-hand panel of Fig. 11 is a more extreme version of this showing histograms for single-image retrievals that peak at the maximum AGB as well as close to 0 AGB. This is typical for SAR images with a small dynamic range and a model that flattens out at very low AGB and is evident, for example, in tropical rainforests. Consequently, the weighting introduces a bias which depends on how many SAR observations gave AGB estimates close to 0.

To understand the relative performance of the AGB retrieval in the two implementations of BIOMASAR, the estimates of AGB obtained with the C- and L-band data are compared to a common reference, represented by the LiDAR-based canopy height in Fig. 12. Both sets of estimates showed moderate agreement with canopy height but different levels for a given canopy height. The BIOMASAR-L estimates spanned a wider range than those from BIOMASAR-C. For heights below 15 m, the L-band estimates were smaller than those from C-band, especially for the shortest forests where the C-band values appeared unrealistically high. For forests taller than 25 m, the L-band estimates were larger than the C-band estimates and exhibited some sensitivity to canopy height, whereas the C-band values often saturated. In the intermediate range of 15–25 m, the estimates by BIOMASAR-C and -L were comparable. The large spread of the AGB estimates for a given canopy height bin was partly due to the sparse sampling of canopy height within a 1 km^2 pixel compared to the spatially explicit nature of the AGB estimates.

As anticipated from Fig. 12, the merging weighted the C- and L-band datasets almost equally (Fig. 13) except for: (i) tropical rainforests, where it relied exclusively on the BIOMASAR-L AGB estimates due to under-prediction by BIOMASAR-C and (ii) short forests and vegetation, where the proportion of BIOMASAR-L AGB estimates dominated.

Although the dataset of satellite images used to estimate AGB each year consisted of the same type of observations, year-to-year fluctuations of the estimates unrelated with accumulation or losses of biomass were expected because of noise and the weak sensitivity of the backscatter observations to AGB. Fig. 14 shows the temporal standard deviation of the annual AGB estimates between 2015 and 2021. This was mostly below 15 Mg ha^{-1} and increased slightly with tree cover because of the decreasing sensitivity to AGB in denser forest. An analysis of the reliability of the AGB changes is deferred to a later study.

The set of AGB estimates for 2020 obtained with the CCI Biomass algorithm is displayed in Fig. 15. Examples of AGB maps at full resolution are also included in Fig. S12 and highlight the spatial detail in the AGB dataset. The highest AGB (>300 Mg ha^{-1}) was obtained in the

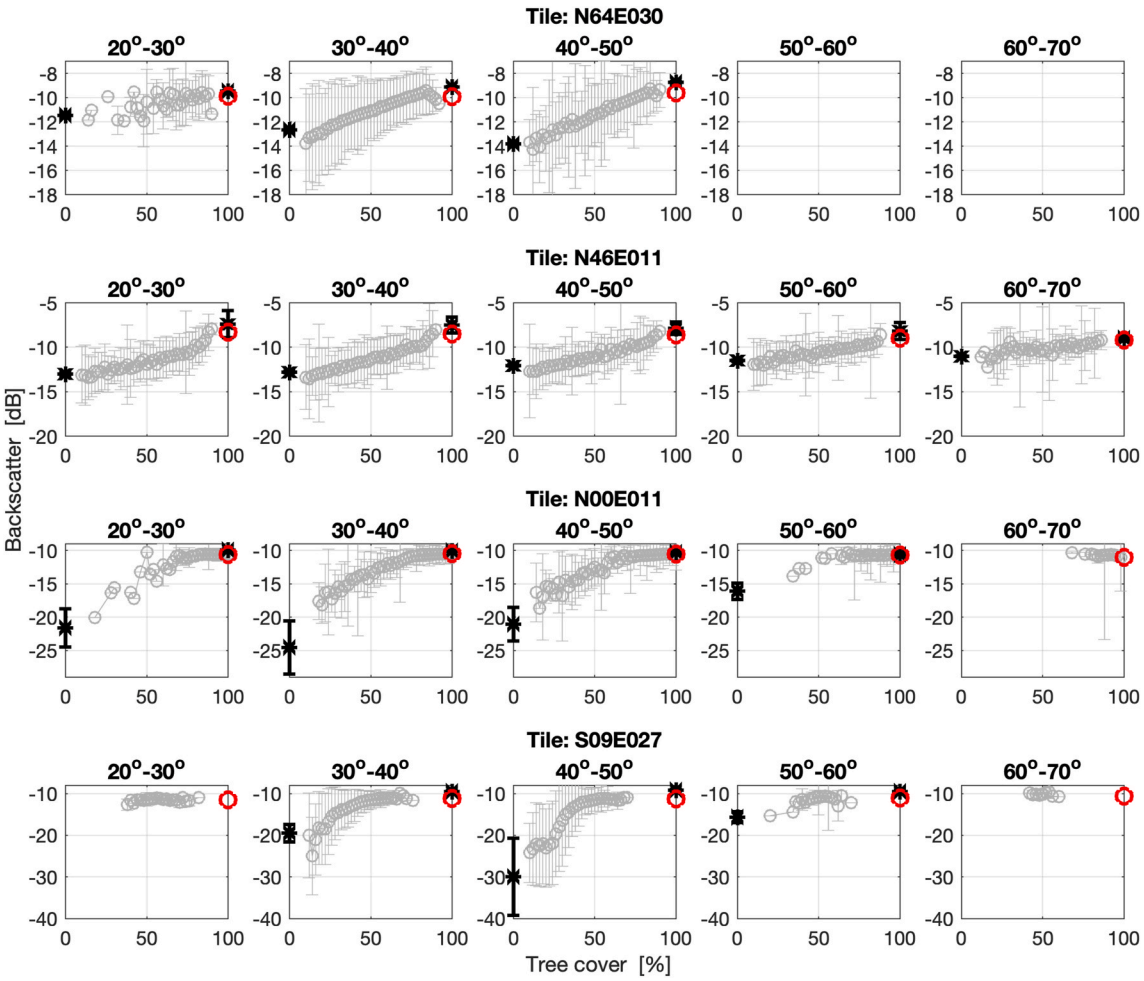

Fig. 10. Observations of tree cover density and ALOS-2 backscatter stratified by tile (rows) and by incidence angle range (columns). Grey circles and vertical bars represent the median value and the range of values per tree cover bin. The asterisks at tree cover 0% and 100% together with their vertical bars in black represent the estimates of σ^0_{gr} and σ^0_{veg}, respectively, and their SD for the given tile and incidence angle range. Red circles represent the initial estimate of σ^0_{df}. The SAR backscatter data consist of ALOS-2 PALSAR-2, HV-polarization observations acquired during July 2020. Blank panels refer to cases not represented in the datasets. (For interpretation of the references to color in this figure legend, the reader is referred to the Web version of this article.)

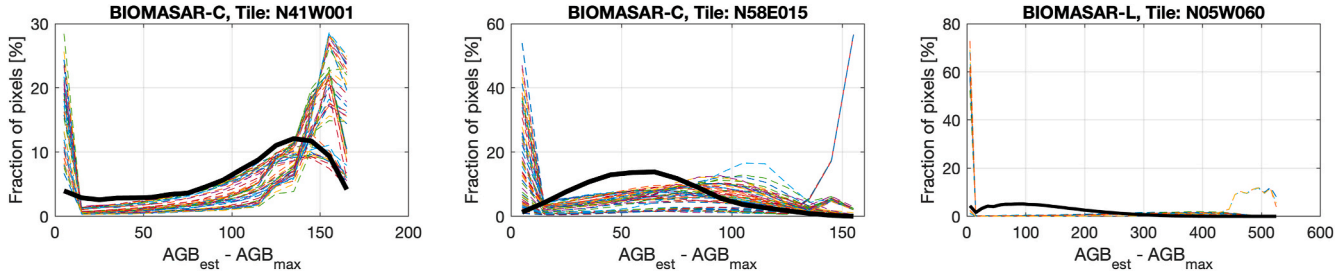

Fig. 11. Tile-based histograms of retrieved AGB from single SAR images using Eq. (5) (dashed curves) and from their weighted average using Eq. (7) (solid curves). The histograms are plotted as a function of the difference between estimated AGB and maximum AGB in the tile.

tropical rainforests of South America, Africa and Southeast Asia, in temperate rainforest of the Pacific Northwest between Canada and the U.S., in southern Australia, and along the Andes between Chile and Argentina. AGB decreased from temperate and tropical to boreal forest in the northern hemisphere, while the southern hemisphere displays a decrease corresponding to the transition from tropical wet to tropical dry forest and savannah vegetation.

4.4. Standard deviation of the AGB estimates

The precision of the two parameters in Eq. (4) relating canopy height to AGB was quite variable. The SD of the p_1 values lay between 10% and 206% of the estimate, whereas the SD of p_2 was largerly below 20% but at most 35% of the estimated value (Fig. 7). In contrast, the precision of the parameter q in (Eq. (3)) was below 5% of the estimated value because of the tight correlation between canopy height and canopy density (Kay et al., 2021).

For the forest backscatter model parameters, the SD was between

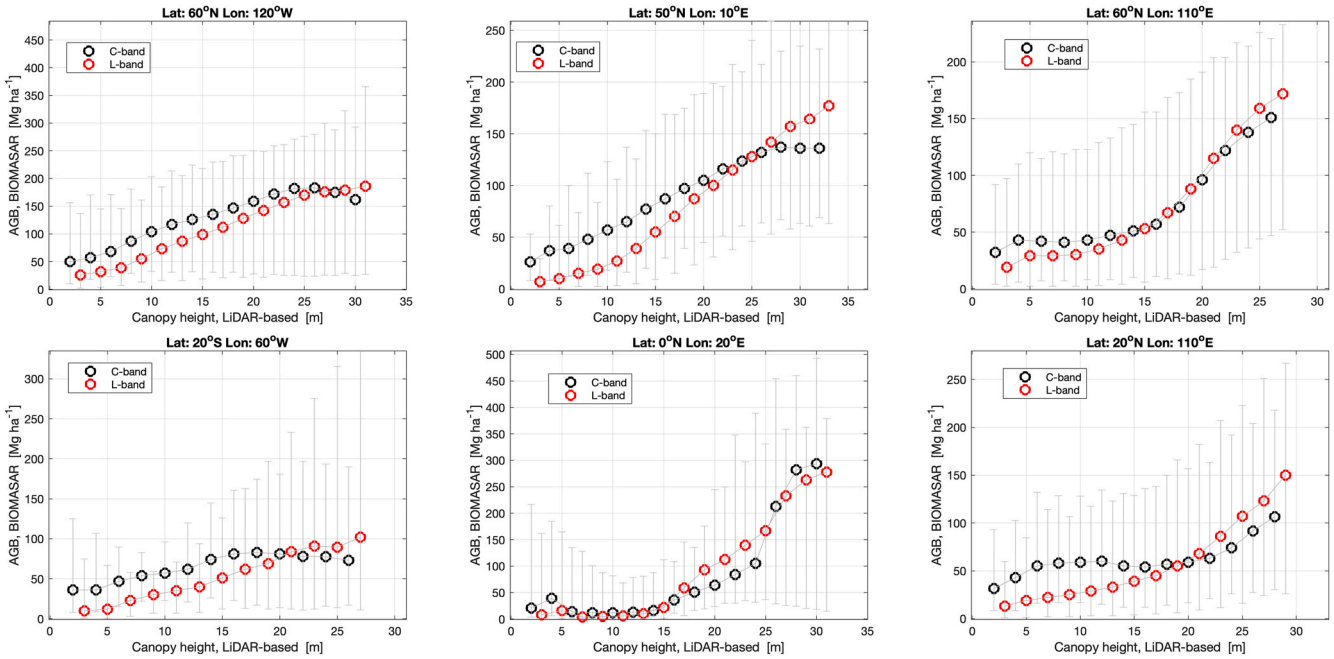

Fig. 12. Distribution of BIOMASAR-C and BIOMASAR-L AGB estimates per canopy height bin for areas across the boreal and temperate zones (top row), and the tropical and subtropical zones. Each area covers 20° × 20° and is centered at the location reported above the corresponding panel. Circles and vertical bars represent the median value and the 5th-95th percentile interval of AGB estimates, respectively, for a given bin of canopy height. Each bin of canopy height is 2 m wide. AGB and canopy height values in these plots are average values for 1 km^2 pixels.

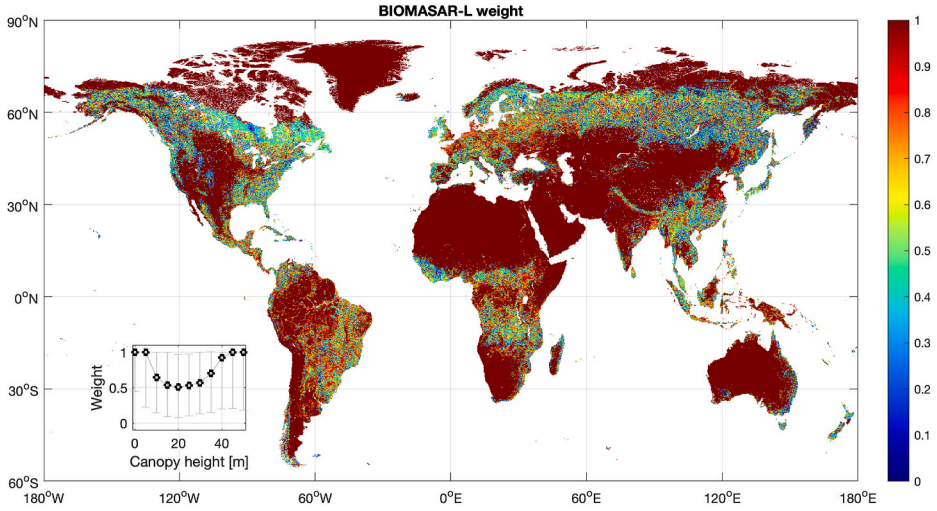

Fig. 13. Map of the weights applied for the BIOMASAR-L AGB estimates. The inset shows the distribution of the weights as a function of canopy height. For each bin of canopy height, the circle and the vertical bar represent the median and the interval between the 5th and the 95th percentile of the weights.

30% and 50% of the estimated value for σ^0_{gr} and around 10% for σ^0_{veg} at C-band (Fig. 9). At L-band, it ranged between 10% and 40% of the estimated value for σ^0_{gr} and was around 5% for σ^0_{veg} (Fig. 10). For the two-way signal attenuation coefficient, α, we assumed a standard deviation of 0.25 dB/m, which is roughly consistent with the range of values reported in the literature (Chauhan et al., 1991; Kurum et al., 2009; Praks et al., 2012; Sheen et al., 1994; Shinohara et al., 1992; Ulaby et al., 1990).

Fig. 16 shows an example of correlation of the errors r_{ij} in Eq. (17) between AGBs derived from pairs of Sentinel-1 monthly composites. It was moderate for images acquired along the same or adjacent orbital tracks, regardless of the month of acquisition of the images, and was close to zero for images acquired along different orbital directions. Although the LiDAR-based datasets included a wide variety of forest types and structural conditions, we did not observe dependency of the error correlation on seasonal conditions or polarization. For C-band, the median of all temporal correlations of AGB was 0.52. A similar value of 0.5 was obtained for L-band, even though the L-band dataset was not as temporally dense. These two constant error correlation values were eventually used.

Knowing all SDs and the error correlation allowed the SD of the AGB estimated from a backscatter measurement and, thereof, the SD of the multi-temporal AGB estimate from Eq. (11) to be quantified. Fig. 17 shows an example of an AGB map from BIOMASAR-C and the corresponding SD values, together with the components of the SD. The spatial distribution of AGB compares well to the distribution of tree cover. The

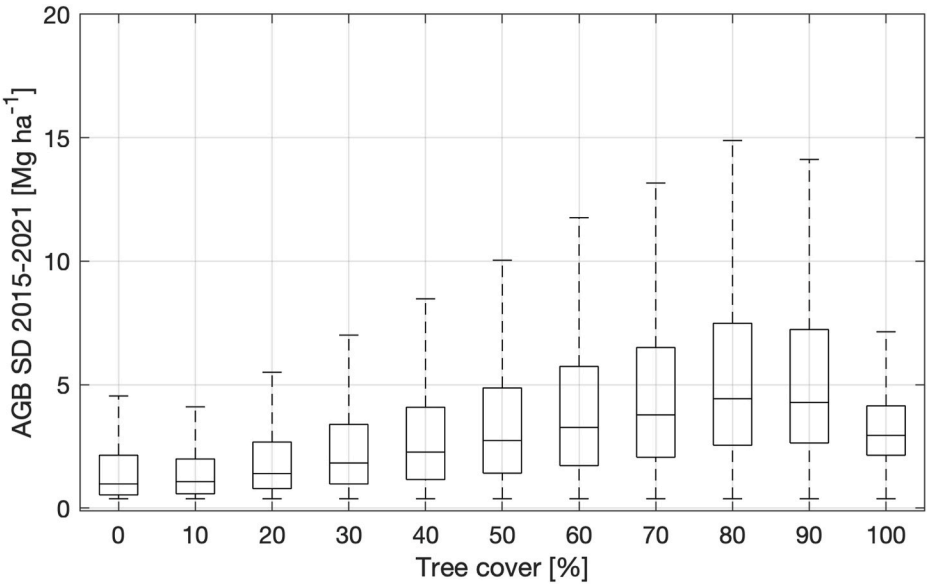

Fig. 14. Standard deviation in time for the set of AGB estimates between 2015 and 2021, stratified by the tree cover. Each box refers to the interquartile range of standard deviation values with the central marker being the median value. The whiskers extend to the most extreme data points not considered outliers. The outliers, defined as data points away from the median by at least three standard deviations, are not plotted because these are associated with forest cover changes.

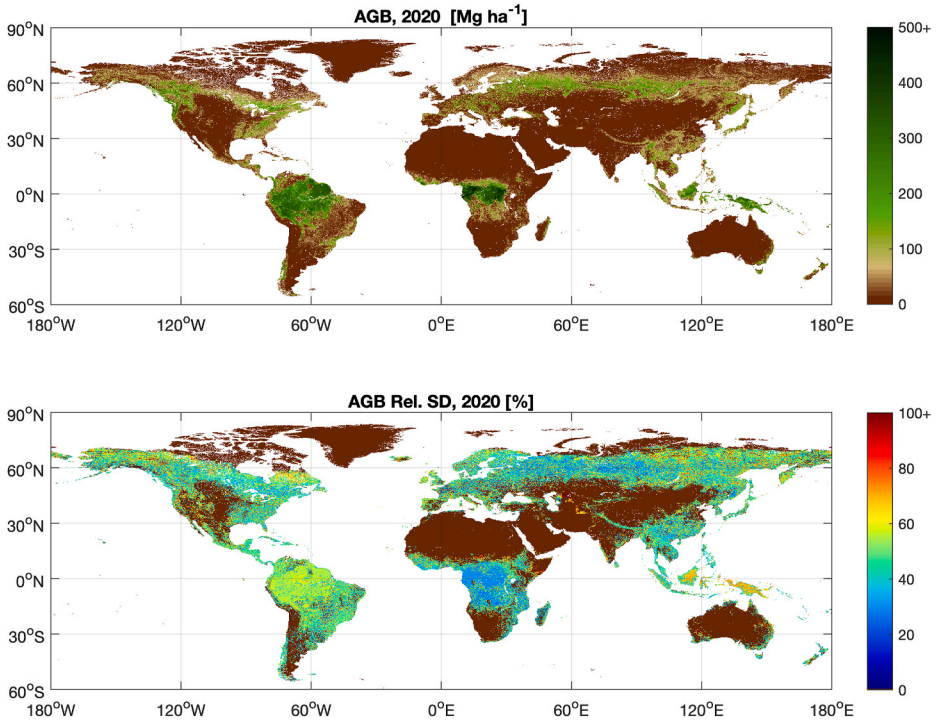

Fig. 15. AGB and AGB SD estimates for 2020 with a spatial resolution of 100 m. The AGB values are clipped between 0 and 500 Mg ha^{-1} to enhance color contrast. Likewise, the AGB relative SD values are clipped between 0% and 100% of the estimated AGB. (For interpretation of the references to color in this figure legend, the reader is referred to the Web version of this article.)

SD of AGB roughly scaled with AGB, being around 80% of the estimated AGB in this example. Because of the moderate value used for the temporal correlation of errors, the AGB SD was driven by the error covariance component. For Sentinel-1, the covariance term was much larger than the variance term, not least because the large number of Sentinel-1 observations used to estimate AGB reduced the variance term. Similar results were obtained for BIOMASAR-L even though the difference between the variance and the covariance component was not as large due to the smaller number of observations (not shown here).

The SD of the AGB estimates obtained from merging the C- and L-band values was still substantial (Fig. 15), being on average 50% and mostly between 30% and 85% of the estimated AGB. It was affected by the proportion of C- and L-band estimates used. For the wet tropics, where the estimate depended solely on L-band data, the SD was about 30%, 50% and 70% of the estimated AGB in Africa, South America and Southeast Asia, respectively. In extra-tropical regions, where the AGB estimates combined values from both SAR frequencies, the SD was around 30–40% of the estimated value. The striping, particularly

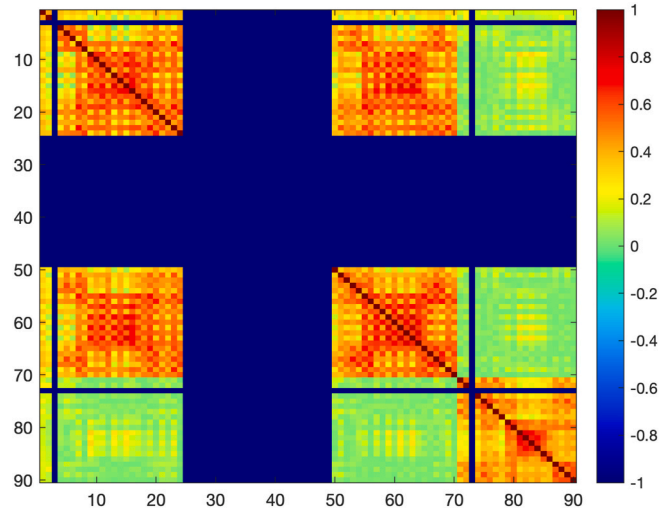

Fig. 16. Matrix of error correlations for Sentinel-1 AGB estimates for the NEON CHEQ site in the U.S. located at 90°W, 45°N. The index on each axis represents the sequential index of each monthly backscatter average covering the site (i.e., 1, 2, 3 etc. mean first, second, third, etc. average image in 2017). Odd integers refer to VH-polarized images. Even integers refer to VV-polarized images. The correlation matrix shows several blocks, each corresponding to a set of 24 images (i.e., 12 months and 2 polarizations) from a given orbital track covering the site. Empty blocks imply that the two orbital tracks being correlated did not have any overlap.

evident in northern regions of Canada and Russia, is a consequence of the rather low and uneven number of observations at C- and L-band (Figs. 1 and 2).

4.5. Verification of the AGB estimates

The uneven spatial distribution of the plot inventory data (Fig. S6) did not allow a global validation of the AGB estimates. Tier 1 grid cell averages were used to identify systematic anomalies in the retrieval algorithm, whereas Tier 2 and 3 plot-based values provided indications on the retrieval accuracy, even if the results must be understood as being local.

Fig. 18 compares map-based and plot-based Tier 1 grid cell averages split by countries, regions or biomes (Fig. S6). It conveys that the spatial distribution of AGB has been well captured globally (Fig. 18). However, dispersion and under-prediction of AGB are evident in many regions as indicated by the relative RMSD values, which were between 36% and 80%. These results mainly come from dispersion except for India and Tasmania, where they were a consequence of the large bias. Large biases also occurred for other regions (Yucatan, Guyana, West and East Africa, Mozambique, Madagascar, Nepal and Western Australia), where the dispersion was more moderate than in regions with lower biases (e.g., Alaska, Nova Scotia, Sweden, Croatia).

Fig. 18 indicates that retrieval performance differed depending on the region. The strongest agreement between reference and map-based values was obtained for three regions with completely different forest structures and AGB levels (tropical forests of the Amazon and the Congo Basins and forests in China and Spain). The few cases of over-prediction occurred for AGB below 100 Mg ha^{-1} both in boreal (Nova Scotia and Sweden) and tropical (Laos & Vietnam) forests. The more common under-prediction started at different levels of reference AGB and was not related to climatic or forest conditions. Almost the whole of Yucatan, Guyana, the Netherlands, Croatia, Mozambique, India, Nepal, Western Australia and Tasmania exhibited under-prediction, while under-prediction only in the high AGB range occurred in Sweden, West and East Africa and East Australia.

At Tier 2 and 3 levels, the map-based and plot-based AGBs agreed albeit a substantial dispersion along the identity line (Fig. 19) in particular for the Tier 2 data, as shown by the larger relative RMSD compared to Tier 3 and the similar bias values. Both under- and over-prediction occurred up to 400 Mg ha^{-1} although mostly moderate (Fig. 19). Under-prediction instead characterized plots with AGBs >400 Mg ha^{-1}, thus explaining for both Tiers the negative bias. For the Tier 2 plots with AGB >700 Mg ha^{-1}, which were mostly located in Tasmania, the retrieval algorithm did not detect any sensitivity and underestimated

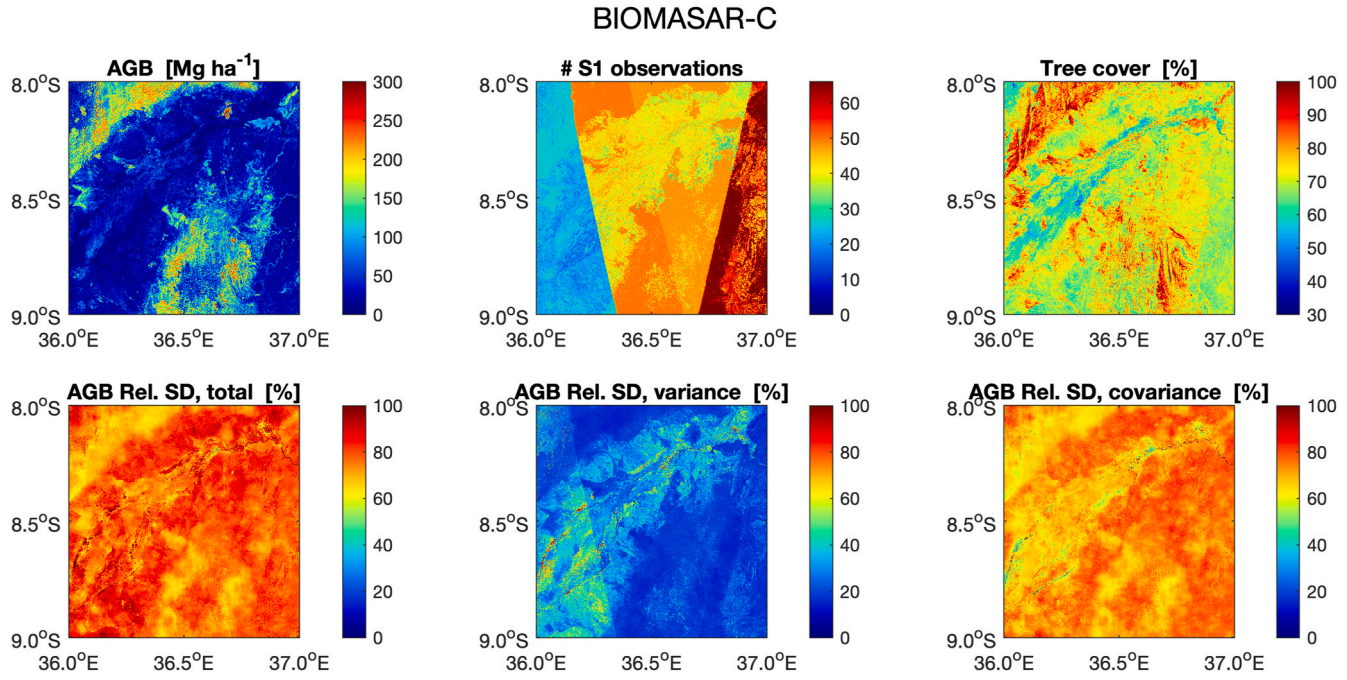

Fig. 17. AGB estimates from BIOMASAR-C, number of Sentinel-1 monthly averages in 2020 and contextual information from the Landsat tree cover dataset for a 1° × 1° tile in the top row. The bottom row shows the maps of AGB SD together with its variance and covariance terms. These panels express SDs relative to the estimated AGB.

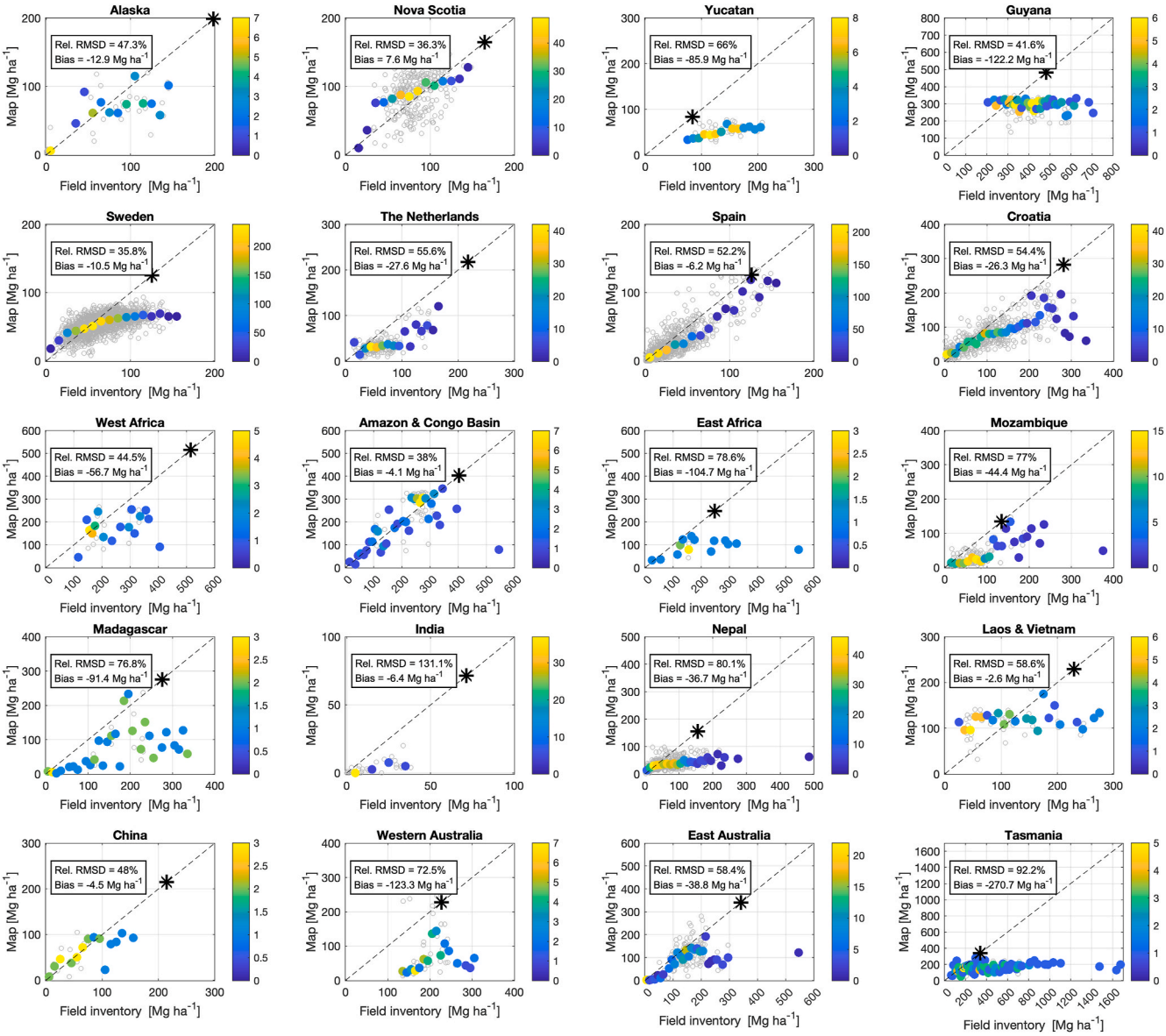

Fig. 18. Comparisons between map-based and plot-based AGB values for Tier 1 plot data spatially averaged to 0.1° (grey circles). The data are grouped per region (see Fig. S13). In each panel, the map-based AGBs were also binned over 10 Mg ha^{-1} wide ranges with filled circles representing the median mapped AGB per bin. The color bars represent the number of grid cells within a given AGB interval. Each panel includes the root mean square difference (RMSD) between map and field inventory AGB relative to the mean value of the reference AGB and the bias, i.e. the difference between mean values of the map AGB and the reference AGB. The asterisks on the identity line represent the maximum AGB in each region. (For interpretation of the references to color in this figure legend, the reader is referred to the Web version of this article.)

AGB by a factor 2 to 5.

5. Discussion

5.1. Data

The development of the global AGB retrieval approach was driven by repeated satellite data that are available globally with high-to moderate spatial resolution and some sensitivity to forest structure. As a result, the pool of observations was restricted to data from four sensors, two SAR sensors capable of wall-to-wall repeat coverage on an annual basis (Figs. 1 and 2) together with sampled data from two spaceborne LiDAR missions. Spatially explicit estimation of AGB exploited C- and L-band backscatter from imaging sensors. At these frequencies, the sensitivity of radar backscatter to forest structural properties is mostly related to tree cover (Figs. 9 and 10), and a more suitable biomass predictor would be from single-pass SAR interferometry that, similarly to laser instruments, generates observations containing information on the vertical and horizontal distribution of vegetation. Estimating canopy height from interferometric elevation requires knowledge of the terrain elevation and the degree of penetration of the microwaves into the canopy (Walker et al., 2007). The lack of global digital surface models and partial knowledge of scattering mechanisms in forest canopies currently prevent this.

Unlike interferometric datasets, the signal recorded by a laser instrument contains a ground return, so an external terrain elevation dataset is not required to estimate vegetation height. In addition, the signals acquired by spaceborne LiDAR systems are better understood and their availability make them a prominent candidate to support global estimation of AGB. The sampling nature of spaceborne LiDAR data, however, means that even after several years of acquisitions, the coverage is not wall-to-wall and their greatest value is in calibrating

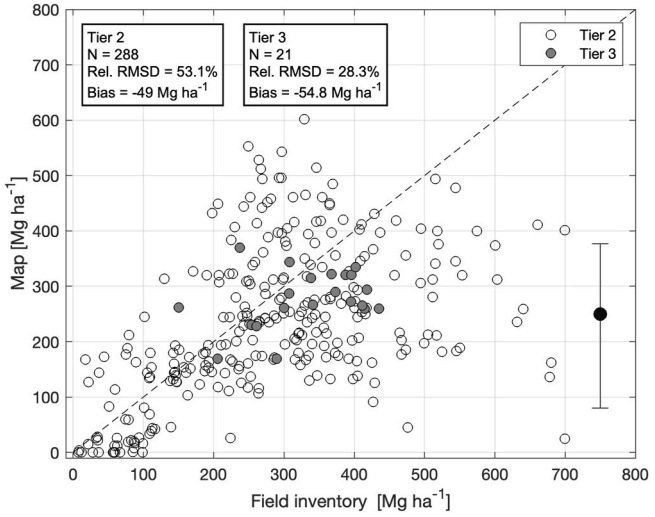

Fig. 19. Map-based and inventory-based AGB values for Tier 2 and 3 data. To improve presentation, axes are truncated at 700 Mg ha^{-1}. The distribution of map-based AGBs for inventory-based values greater than 700 Mg ha^{-1} are represented by the filled circle (median value) and the vertical bar (5th to 95th percentile) at AGB = 750 Mg ha^{-1}.

some elements of the AGB retrieval model rather than providing the model itself.

We exploited the global observing capabilities of ICESat and ICESat-2 data in preference to GEDI data, despite GEDI being designed to observe terrestrial vegetation. Hence, our AGB estimates are independent of those obtained by GEDI (Duncanson et al., 2022) which assists understanding of the strengths and weaknesses of their respective retrieval models (Hunka et al., 2023). However, regardless of the LiDAR system, the structural metrics derived from the observations still suffer from uncertainties due to mechanisms that are only partly understood (Milenković et al., 2022; Neuenschwander and Pitts, 2019). For example, despite strong filtering to remove outliers, unrealistically high values of canopy height are observed in sparsely vegetated regions (Fig. 4). Additional filtering would cause large gaps in very dense forests where the lidar datasets used here already miss a large proportion of samples (Fig. 4). Such uncertainties propagate through the retrieval chain, affecting among others the maximum canopy height and maximum AGB, which is a strong control on the performance of the AGB retrieval. Our definition of the maximum canopy height was effectively constrained by the noise in the ICESat-2 dataset and the sparse sampling after filtering. This led to underestimation of the maximum AGB in some regions (Fig. 18). A wider set of samples from spaceborne LiDAR and better knowledge of their properties will likely improve the dataset of canopy heights and reduce the uncertainty of the maximum canopy height estimates.

5.2. Methods

The model relating canopy height to AGB is less characterized than the structural model relating canopy height and canopy density (Kay et al., 2021) because a global dataset of reference AGB values is unavailable. Spatial representativeness could only be achieved at the expense of spatial detail by using AGB average values at subnational level from NFIs. The predictions from the generalized structural models broadly agree with the dataset of reference AGB values (Fig. 8) thanks to the balancing of the NFI-based averages across the 17 strata (Fig. 7). However, the validation raises some issues on bias. In addition, the SDs of the model parameters occasionally exceeded 100% of the estimated values, implying considerable uncertainty in the structural models, which can be primarily related to the quality of the reference AGB data. The NFI statistics were not harmonized with each other, and there are differences in the definitions of forest land underlying the NFI average values. The strata used to group the NFI data were based on macro-ecological patterns, which smoothed out small scale variability in the relationship between canopy height and AGB, for example due to spatial variability of wood density or growth factors. In addition, the use of average values instead of AGB measured in plots and footprints may alter the shape of the model, leading to over- or under-estimates when applied at the spatial resolution of the satellite image data.

Quantifying the impact of a mismatch of spatial scales was attempted by comparing our generalized structural model with the few regional models published in the literature, which were based on collections of field measurements taken at sub-hectare scale (Fig. S10, left hand side). The AGBs predicted by the two realizations of the structural model were different, in particular in extra-tropical regions. The uncertainty of the modeled backscatter caused by the choice of structural model was comparable to the uncertainty of the backscatter measurements (i.e., $<$0.5 dB, Fig. S10, top right panel). Only when the AGBs predicted by the structural models differed by more than 100% (Fig. S10, bottom left panel) did the Water Cloud Model associate a manyfold difference in terms of AGB for a given level of the SAR backscatter (Fig. S10, bottom right panel). Future studies should consolidate these indications and assess to which degree the final estimates of AGB are affected by the spatial characterization of the structural function.

Despite its simple formulation, the retrieval model was able to reproduce the relationship between AGB and SAR backscatter at C- and L-band (Figs. 9 and 10). Tile-by-tile estimation of the model parameters and stratification of the estimation by incidence angle range helped to adapt the retrieval to local conditions. Nonetheless, the weak correlation between SAR backscatter and forest variables resulted in considerable dispersion in the estimates (Figs. 9 and 10). The model parameters, in particular σ^0_{gr}, had uncertainties manifesting either as biases compared to more realistic values (see tile S09E027 in Fig. 9) or large standard deviations (see tile N00E011 in Fig. 10).

Caveats associated with the AGB retrievals at each frequency (Fig. 12) motivated the merging of AGB estimates using a procedure designed to account for the physics behind the relationship relating forest structure and radar backscatter. Favoring L-band estimates of AGB for the lowest and highest AGBs (Fig. 14) while balancing the estimates in the intermediate range helps to avoid systematic errors that would affect an AGB dataset based on either the C- or the L-band observations. Although the objective of this paper is not to investigate the temporal features of the AGB estimates, we found little variability in the AGB values over time (Fig. 13), thus building confidence in the temporal trajectories of repeated AGB estimates. Keeping the design of the merging approach simple, however, implies that only systematic errors are coped with.

Because the retrieval approach is entirely parametric, the estimation process can be split into several basic steps each of which can be tuned. In addition, training the retrieval model without using AGB reference measurements makes it possible to produce a temporal sequence of AGB estimates. However, a consequence is that the retrieval model cannot be adapted to local conditions finer than a certain spatial scale (e.g., 1°). Use of non-parametric machine learning models could perhaps better address local spatial variation but would require spatially dense reference AGB datasets contemporary with the EO predictors. Such datasets are unavailable for most of the planet; nonetheless, recent studies addressing the training data requirements of retrieval models for global applications have laid the foundations for evolution of algorithms in the years to come (Chave et al., 2019; Labrière et al., 2023).

5.3. AGB estimates

Relying on a fully parametric and physics-based approach allowed weaknesses in the approach to be identified and provided indications of the extent to which improvements are possible.

The strong agreement (Fig. 19) for regions with Tier 2 and 3 data and

tropical rainforest (Amazon and Congo Basin), Mediterranean forest (Spain) and mostly subtropical forest (China) (Fig. 18), as well as across some of the boreal forest regions (Alaska and Nova Scotia) indicates that the components of the CCI Biomass retrieval algorithm (structural functions, forest backscatter model and merging) are well configured. Nonetheless, several regions displayed a tendency to under-prediction, arising from a combination of approximations in the calibration of the forest backscatter model and of the structural model that relates canopy height to AGB.

Because of the decreasing sensitivity of backscatter to increasing AGB and the calibration of the retrieval model without field measurements, the retrieval was strongly affected by the data on maximum AGB (Fig. 4). Large under-prediction arose when the estimated maximum AGB is considerably lower than the value predicted from the field data (Yucatan, Guyana, Nepal, Western Australia and Tasmania in Fig. 18). This is partly explained by gaps in the ICESat-2 dataset in the tallest forests due either to the sampling (e.g., in Tasmania, the canopy height by ICESat-2 hardly exceeded 40 m, Fig. 4e) or the strong filtering that removed likely realistic values of canopy height. Another reason is that the structural model relating canopy height to AGB in Eq. (4) is poorly constrained, as was the case for Central Asia and Southeast Asia in Fig. 7. Finally, the coarse characterization of the structural model explains the non-systematic under-prediction in a few regions (e.g., the Netherlands, Croatia, West Africa, Mozambique and East Australia). While an estimate of maximum AGB cannot be avoided, the retrieval should advance use of this information beyond treating it solely as a cut-off value.

Imperfect calibration of the forest backscatter model explained cases where the estimated AGB flattened out for increasing AGB (Sweden, Yucatan, Guyana, East Africa, Madagascar and Laos & Vietnam in Fig. 18). Here, the histogram of the AGB estimates from the individual SAR images presented either strong bimodality (Guyana and Laos and Vietnam; see, for example, tile N05W060 in Fig. 11) or strong temporal variability (Sweden, East Africa and Madagascar; see, for example, tile N58E015 in Fig. 11). The set-up to calibrate the forest backscatter model is reliable (Figs. 9 and 10), and an error of a fraction of a dB when estimating σ^0_{gr} or σ^0_{veg} may be considered acceptable, but the consequences on the final AGB estimates can be catastrophic as it shifts the whole histogram of AGB values from a given image to considerably lower or higher values.

To get further understanding of the errors, we compared plot-based and map-based AGB estimates from the precursor to this study (Santoro et al., 2021a) (Fig. S14), which was based on a smaller number of SAR observations and a more empirical set of functions relating the observations to AGB. In summary, we identified four systematic patterns, summarized below.

- The estimation of AGB improved at sites in the boreal zone that were characterized by a considerable contribution of the C-band AGB component as a consequence of the cross-polarized Sentinel-1 channel (Alaska, Nova Scotia, Sweden low AGB levels).
- Availability of multi-temporal L-band data improved the AGB estimates in the wet tropics (Amazon & Congo Basin).
- Sites where the values of the maximum AGB differed in this study and in the precursor were characterized by substantial differences in terms of biases (e.g., West Africa, Madagascar, Western Australia). The bias was always a consequence of an incorrect maximum AGB. In Santoro et al. (2021a), the maximum AGB was based on an extrapolation from various datasets. In this study, it was derived from the ICESat-2 metric of canopy height and the height-to-AGB structural function. Both approaches have drawbacks. Noisy values in the ICESat-2 dataset and the coarse resolution of the structural function explain the biases in our estimates. Constraining the estimation of maximum AGB with local information may improve the spatial characterization of this variable.
- The inability of the method to estimate the AGB beyond a certain level in Sweden, Yucatan, Guyana, East Africa, Madagascar (Fig. 18) is likely due to an overestimate of the σ^0_{veg} coefficient at L-band. Its estimation relies on an estimate of canopy density of dense forests using Eq. (9), which leads to an overestimate of σ^0_{veg} when the canopy density of dense forests is underestimated. In Santoro et al. (2021a), this value was derived from a map of canopy density. Here, the canopy density of dense forests was derived with the structural function in Eq. (3) starting from an estimate of the height of dense forests, which relied on the ICESat-2 dataset (Fig. 4). In those regions, we found that the ICESat-2-based canopy density of dense forests was smaller than the value derived from the canopy density map. The sparse spatial sampling of the ICESat-2 dataset might not have represented the population of canopy density values captured by the map and might have led to underestimation of the height, and thereof the canopy density, of dense forests.

The considerable biases and standard deviation affecting the AGB estimates (Fig. 15) are a consequence of the uncertainties affecting the EO predictors (Fig. 3) and the design of the retrieval model. The uncertainty associated with the EO data can be reduced by relying either on data sources that are more closely related to the structural properties of a forest (TanDEM-X interferometry, future BIOMASS mission) or on the same type of backscatter observations considered in this study but with higher radiometric accuracy (future Sentinel-1 Next Generation, ALOS-4 PALSAR-3 and NISAR missions). Algorithmic advances are unlikely to yield a substantial reduction in the model-related part of the uncertainty unless calibration of the models to estimate AGB is aided by spatially dense sets of field measurements.

The validity of the AGB estimates is affected by the limitations of the AGB ground reference data. Historically, NFI data have been developed to assess forest resources, such as growing stock volume, but not to evaluate AGB stocks. The inclusion of NFI methods for AGB assessment is progressing but remains challenging, potentially explaining why the calibration of Eq. (4) is uneven (Fig. 7). A key problem is that most NFI estimates are based on small randomly drawn circular plots or transects, while AGB density estimation is uncertain when the forest inventory plots are smaller than 0.25 ha and when plots have high edge to area ratios (Réjou-Méchain et al., 2014). A second problem is that NFIs are scarce in the tropics and have only been implemented recently in the major tropical forest countries. This results in a latitudinal imbalance in the AGB ground reference data. Permanent inventory plots provide a crucial alternative source of information (Davies et al., 2021; Blundo et al., 2021) especially at the stage of validation, and they can be complemented with airborne laser scanning campaigns, ideally above the sites where inventory plots are available (Chave et al., 2019). The recent GEO-TREES program, which aims to provide biomass reference values from more than 100 forest landscapes and more than 200 supplementary sites world-wide, can help to address this gap (Labrière et al., 2023).

6. Conclusions

We have described and evaluated the CCI Biomass global AGB estimator, which is based on high-to moderate-resolution satellite data. We included an in-depth analysis of factors that affect the AGB estimation, namely satellite data, estimation methods and the use of AGB reference data. The satellite data component is constrained by the availability of repeated wall-to-wall coverage with a spatial resolution of about a hectare. SAR backscatter by Sentinel-1 and ALOS-2 PALSAR-2 are the only global satellite datasets fulfilling this requirement. However, the weak sensitivity of SAR backscatter from these sensors to forest variables means that information on forest structure from satellite LIDAR observations is needed to constrain the retrieval of AGB. Potential estimation biases caused by training the retrieval model with AGB measurements that are unevenly distributed in space were dealt with by using auxiliary spatial data that match the definition of the retrieval model parameters.

Such a generalized approach allows the overall spatial distribution of

AGB in woody vegetation worldwide to be well captured, but with local under- or over-predictions of AGB, and considerable dispersion in the estimates. Availability of repeated, co and cross–polarized SAR backscatter observations at C- and L-band improved the retrieval in boreal and tropical forests, respectively, compared to previous endeavors based on a similar retrieval framework. Novel spaceborne LiDAR observations allow for a fully parametric, physics-based retrieval approach. However, sparse spatial sampling and problems in characterizing LiDAR signals from vegetation are currently limitations that are likely to be overcome as more data becomes available.

The retrieval framework can be extended to other satellite data with the same physical background as those used in this study (e.g., from SAR interferometry or low-frequency SAR). The accuracy of the estimates is likely to improve when they are combined with such observations because they are more sensitive to structural properties of vegetation. The retrieval would furthermore benefit from a global, spatially dense dataset (e.g., such as those collected by NFIs) of reference AGB values, which ideally shared the same measurement protocol and had an open access policy. This would allow the retrieval model to be trained without relying on the approximations and generalizations made here to generate realistic estimates of AGB.

CRediT authorship contribution statement

Maurizio Santoro: Writing – original draft, Supervision, Methodology, Investigation, Formal analysis, Conceptualization. **Oliver Cartus:** Writing – original draft, Supervision, Software, Methodology, Investigation, Formal analysis. **Shaun Quegan:** Writing – review & editing, Supervision. **Heather Kay:** Writing – review & editing, Project administration, Methodology, Investigation, Formal analysis, Conceptualization. **Richard M. Lucas:** Writing – review & editing, Validation, Project administration, Funding acquisition, Conceptualization. **Arnan Araza:** Writing – original draft, Validation, Investigation, Formal analysis, Data curation. **Martin Herold:** Writing – review & editing. **Nicolas Labrière:** Writing – review & editing, Data curation. **Jérôme Chave:** Writing – review & editing. **Åke Rosenqvist:** Writing – review & editing, Resources. **Takeo Tadono:** Writing – review & editing, Resources, Data curation. **Kazufumi Kobayashi:** Resources, Data curation. **Josef Kellndorfer:** Writing – review & editing, Software, Data curation. **Valerio Avitabile:** Writing – review & editing, Data curation. **Hugh Brown:** Writing – review & editing, Data curation. **João Carreiras:** Writing – review & editing, Data curation. **Michael J. Campbell:** Writing – review & editing, Data curation. **Jura Cavlovic:** Writing – review & editing, Data curation. **Polyanna da Conceição Bispo:** Writing – review & editing, Data curation. **Hammad Gilani:** Writing – review & editing, Data curation. **Mohammed Latif Khan:** Writing – review & editing, Data curation. **Amit Kumar:** Writing – review & editing, Data curation. **Simon L. Lewis:** Writing – review & editing, Data curation. **Jingjing Liang:** Writing – review & editing, Data curation. **Edward T.A. Mitchard:** Writing – review & editing, Data curation. **Ana María Pacheco-Pascagaza:** Writing – review & editing, Data curation. **Oliver L. Phillips:** Writing – review & editing, Data curation. **Casey M. Ryan:** Writing – review & editing, Data curation. **Purabi Saikia:** Writing – review & editing, Data curation. **Dmitry Schepaschenko:** Writing – review & editing, Data curation. **Hansrajie Sukhdeo:** Writing – review & editing, Data curation. **Hans Verbeeck:** Writing – review & editing, Data curation. **Ghislain Vieilledent:** Writing – review & editing, Data curation. **Arief Wijaya:** Writing – review & editing, Data curation. **Simon Willcock:** Writing – review & editing, Data curation. **Frank Martin Seifert:** Writing – review & editing, Supervision.

Declaration of competing interest

The authors declare that they have no known competing financial interests or personal relationships that could have appeared to influence the work reported in this paper.

Data availability

Data will be made available on request.

Acknowledgments

This research was supported by the European Space Agency with ESRIN contract no. no. 4000123662/18/I-NB (Climate Change Initiative BIOMASS project) and, in part, contract 4000138809/22/I-DT-BGH (BiomAP, Integrating Active and Passive microwave data towards a novel global record of above-ground biomass maps). We thank the CCI Biomass project team for valuable suggestions and stimulating scientific discussions. All satellite datasets have a free and open data policy access except for the ALOS-2 PALSAR-2 datasets which were made available by JAXA to a restricted number of users as part of the Kyoto and Carbon (K&C) Initiative (https://www.eorc.jaxa.jp/ALOS/en/activity/kc_e.htm) and under the collaboration between ESA and JAXA in the CCI Biomass project. The ICESat-2 ATL08 Version 5 data product was retrieved from the National Snow and Ice Data Center (NSIDC) (https://nsidc.org/data/atl08/versions/5#anchor-0). The dataset of tree cover was released by the United States Geological Survey (USGS) and the University of Maryland, Department of Geographical Sciences, (https://glad.umd.edu/dataset/global-2010-tree-cover-30-m). The CCI Land Cover dataset, version 2.1 was obtained from https://maps.elie.ucl.ac.be/CCI/viewer/. The Copernicus DEM was derived from the WorldDEM produced from interferometric X-band SAR observations from the German TanDEM-X satellite mission (https://spacedata.copernicus.eu/collections/copernicus-digital-elevation-model).

Appendix A. Supplementary data

Supplementary data to this article can be found online at https://doi.org/10.1016/j.srs.2024.100169.

References

Araza, A., de Bruin, S., Herold, M., Quegan, S., Labriere, N., Rodriguez-Veiga, P., Avitabile, V., Santoro, M., Mitchard, E.T.A., Ryan, C.M., Phillips, O.L., Willcock, S., Verbeeck, H., Carreiras, J., Hein, L., Schelhaas, M.-J., Pacheco-Pascagaza, A.M., da Conceição Bispo, P., Laurin, G.V., Vieilledent, G., Slik, F., Wijaya, A., Lewis, S.L., Morel, A., Liang, J., Sukhdeo, H., Schepaschenko, D., Cavlovic, J., Gilani, H., Lucas, R., 2022. A comprehensive framework for assessing the accuracy and uncertainty of global above-ground biomass maps. Remote Sens. Environ. 272, 112917. https://doi.org/10.1016/j.rse.2022.112917.

Askne, J., Dammert, P.B.G., Ulander, L.M.H., Smith, G., 1997. C-band repeat-pass interferometric SAR observations of the forest. IEEE Trans. Geosci. Remote Sens. 35, 25–35. https://doi.org/10.1109/36.551931.

Askne, J., Santoro, M., 2005. Multitemporal repeat pass SAR interferometry of boreal forests. IEEE Trans. Geosci. Remote Sens. 43, 1219–1228. https://doi.org/10.1109/TGRS.2005.846878.

Asner, G.P., Mascaro, J., 2014. Mapping tropical forest carbon: calibrating plot estimates to a simple LiDAR metric. Remote Sens. Environ. 140, 614–624. https://doi.org/10.1016/j.rse.2013.09.023.

Avitabile, V., Herold, M., Henry, M., Schmullius, C., 2011. Mapping biomass with remote sensing: a comparison of methods for the case study of Uganda. Carbon Balance Manag 6, 7. https://doi.org/10.1186/1750-0680-6-7.

Baccini, A., Goetz, S.J., Walker, W.S., Laporte, N.T., Sun, M., Sulla-Menashe, D., Hackler, J., Beck, P.S.A., Dubayah, R., Friedl, M.A., Samanta, S., Houghton, R.A., 2012. Estimated carbon dioxide emissions from tropical deforestation improved by carbon-density maps. Nat. Clim. Change 2, 182–185. https://doi.org/10.1038/nclimate1354.

ForestPlots.net, Blundo, C., Carilla, J., Grau, R., Malizia, A., Malizia, L., Osinaga-Acosta, O., Bird, M., Bradford, M., Catchpole, D., Ford, A., Graham, A., Hilbert, D., Kemp, J., Laurance, S., Laurance, W., Ishida, F.Y., Marshall, A., Waite, C., Woell, H., Bastin, J.-F., Bauters, M., Beeckman, H., Boeckx, P., Bogaert, J., De Canniere, C., De Haulleville, T., Doucet, J.-L., Hardy, O., Hubau, W., Kearsley, E., Verbeeck, H., Vleminckx, J., Brewer, S.W., Alarcón, A., Araujo-Murakami, A., Arets, E., Arroyo, L., Chavez, E., Fredericksen, T., Villaroel, R.G., Sibauty, G.G., Killeen, T., Licona, J.C., Lleigue, J., Mendoza, C., Murakami, S., Gutierrez, A.P., Pardo, G., Peña-Claros, M., Poorter, L., Toledo, M., Cayo, J.V., Viscarra, L.J., Vos, V., Ahumada, J., Almeida, E., Almeida, J., De Oliveira, E.A., Da Cruz, W.A., De Oliveira, A.A., Carvalho, Fabrício Alvim, Obermuller, F.A., Andrade, A., Carvalho, Fernanda Antunes, Vieira, S.A.,

Aquino, A.C., Aragão, L., Araújo, A.C., Assis, M.A., Gomes, J.A.M.A., Baccaro, F., De Camargo, P.B., Barni, P., Barroso, J., Bernacci, L.C., Bordin, K., De Medeiros, M.B., Broggio, I., Camargo, J.L., Cardoso, D., Carniello, M.A., Rochelle, A.L.C., Castilho, C., Castro, A.A.J.F., Castro, W., Ribeiro, S.C., Costa, F., De Oliveira, R.C., Coutinho, I., Cunha, J., Da Costa, L., Da Costa Ferreira, L., Da Costa Silva, R., Da Graça Zacarias Simbine, M., De Andrade Kamimura, V., De Lima, H.C., De Oliveira Melo, L., De Queiroz, L., De Sousa Lima, J.R., Do Espírito Santo, M., Domingues, T., Dos Santos Prestes, N.C., Carneiro, S.E.S., Elias, F., Eliseu, G., Emilio, T., Farrapo, C.L., Fernandes, L., Ferreira, G., Ferreira, J., Ferreira, L., Ferreira, S., Simon, M.F., Freitas, M.A., García, Q.S., Manzatto, A.G., Graça, P., Guilherme, F., Hase, E., Higuchi, N., Iguatemy, M., Barbosa, R.I., Jaramillo, M., Joly, C., Klipel, J., Do Amaral, I.L., Levis, C., Lima, A.S., Dan, M.L., Lopes, A., Madeiros, H., Magnusson, W. E., Dos Santos, R.M., Marimon, B., Junior, B.H.M., Grillo, R.M.M., Martinelli, L., Reis, S.M., Medeiros, S., Meira-Junior, M., Metzker, T., Morandi, P., Do Nascimento, N.M., Moura, M., Müller, S.C., Nagy, L., Nascimento, H., Nascimento, M., Lima, A.N., De Araújo, R.O., Silva, J.O., Pansonato, M., Sabino, G. P., De Abreu, K.M.P., Rodrigues, P.J.F.P., Piedade, M., Rodrigues, D., Rodrigues Pinto, J.R., Quesada, C., Ramos, E., Ramos, R., Rodrigues, P., De Sousa, T.R., Salomão, R., Santana, F., Scaranello, M., Bergamin, R.S., Schietti, J., Schöngart, J., Schwartz, G., Silva, N., Silveira, M., Seixas, C.S., Simbine, M., Souza, A.C., Souza, P., Souza, R., Sposito, T., Junior, E.S., Do Vale, J.D., Vieira, I.C.G., Villela, D., Vital, M., Xaud, H., Zanini, K., Zartman, C.E., Ideris, N.K.H., Metali, F.B.H., Salim, K.A., Saparudin, M.S., Serudin, R.M., Sukri, R.S., Begne, S., Chuyong, G., Djuikouo, M.N., Gonmadje, C., Simo-Droissart, M., Sonké, B., Taedoumg, H., Zemagho, L., Thomas, S., Baya, F., Saiz, G., Espejo, J.S., Chen, D., Hamilton, A., Li, Y., Luo, T., Niu, S., Xu, H., Zhou, Z., Álvarez-Dávila, E., Escobar, J.C.A., Arellano-Peña, H., Duarte, J.C., Calderón, J., Bravo, L.M.C., Cuadrado, B., Cuadros, H., Duque, A., Duque, L.F., Espinosa, S.M., Franke-Ante, R., García, H., Gómez, A., González-M, R., Idárraga-Piedrahíta, Á., Jimenez, E., Jurado, R., Oviedo, W.L., López-Camacho, R., Cruz, O.A.M., Polo, I.M., Paky, E., Pérez, K., Pijachi, A., Pizano, C., Prieto, A., Ramos, L., Correa, Z.R., Richardson, J., Rodríguez, E., Rodriguez, M.G.M., Rudas, A., Stevenson, P., Chudomelová, M., Dancak, M., Hédl, R., Lhota, S., Svatek, M., Mukinzi, J., Ewango, C., Hart, T., Yakusu, E.K., Lisingo, J., Makana, J.-R., Mbayu, F., Toirambe, B., Mukendi, J.T., Kvist, L., Nebel, G., Báez, S., Céron, C., Griffith, D.M., Andino, J.E.G., Neill, D., Palacios, W., Peñuela-Mora, M.C., Rivas-Torres, G., Villa, G., Demissie, S., Gole, T., Gonfa, T., Ruokolainen, K., Baisie, M., Bénédet, F., Betian, W., Bezard, V., Bonal, D., Chave, J., Droissart, V., Gourlet-Fleury, S., Hladik, A., Labrière, N., Naisso, P., Réjou-Méchain, M., Sist, P., Blanc, L., Burban, B., Derroire, G., Dourdain, A., Stahl, C., Bengone, N.N., Chezeaux, E., Ondo, F.E., Medjibe, V., Mihindou, V., White, L., Culmsee, H., Rangel, C.D., Horna, V., Wittmann, F., Adu-Bredu, S., Affum-Baffoe, K., Foli, E., Balinga, M., Roopsind, A., Singh, J., Thomas, R., Zagt, R., Murthy, I.K., Kartawinata, K., Mirmanto, E., Priyadi, H., Samsoedin, I., Sunderland, T., Yassir, I., Rovero, F., Vinceti, B., Hérault, B., Aiba, S.-I., Kitayama, K., Daniels, A., Tuagben, D., Woods, J.T., Fitriadi, M., Karolus, A., Khoon, K.L., Majalap, N., Maycock, C., Nilus, R., Tan, S., Sitoe, A., Coronado, G.I., Ojo, L., De Assis, R., Poulsen, A.D., Sheil, D., Pezo, K.A., Verde, H.B., Moscoso, V.C., Oroche, J.C.C., Valverde, F.C., Medina, M.C., Cardozo, N.D., De Rutte Corzo, J., Del Aguila Pasquel, J., Llampazo, G.F., Freitas, L., Cabrera, D.G., Villacorta, R.G., Cabrera, K.G., Soria, D.G., Saboya, L.G., Rios, J.M.G., Pizango, G.H., Coronado, E.H., Huamantupa-Chuquimaco, I., Huasco, W.H., Aedo, Y. T.H., Peña, J.L.M., Mendoza, A.M., Rodriguez, V.M., Vargas, P.N., Ramos, S.C.P., Camacho, N.P., Cruz, A.P., Arevalo, F.R., Huaymacari, J.R., Rodriguez, C.R., Paredes, M.A.R., Bayona, L.R., Del Pilar Rojas Gonzales, R., Peña, M.E.R., Revilla, N. S., Shareva, Y.C.S., Trujillo, R.T., Gamarra, L.V., Martinez, R.V., Arenas, J.V., Amani, C., Ifo, S.A., Bocko, Y., Boundja, P., Ekoungoulou, R., Hockemba, M., Nzala, D., Fofanah, A., Taylor, D., Bañares-de Dios, G., Cayuela, L., La Cerda, Í.G., Macía, M., Stropp, J., Playfair, M., Wortel, V., Gardner, T., Muscarella, R., Priyadi, H., Rutishauser, E., Chao, K.-J., Munishi, P., Bánki, O., Bongers, F., Boot, R., Fredriksson, G., Reitsma, J., Ter Steege, H., Van Andel, T., Van De Meer, P., Van Der Hout, P., Van Nieuwstadt, M., Van Ulft, B., Veenendaal, E., Vernimmen, R., Zuidema, P., Zwerts, J., Akite, P., Bitariho, R., Chapman, C., Gerald, E., Leal, M., Mucunguzi, P., Abernethy, K., Alexiades, M., Baker, T.R., Banda, K., Banin, L., Barlow, J., Bennett, A., Berenguer, E., Berry, N., Bird, N.M., Blackburn, G.A., Brearley, F., Brienen, R., Burslem, D., Carvalho, L., Cho, P., Coelho, F., Collins, M., Coomes, D., Cuni-Sanchez, A., Dargie, G., Dexter, K., Disney, M., Draper, F., Duan, M., Esquivel-Muelbert, A., Ewers, R., Fadrique, B., Fauset, S., Feldpausch, T. R., França, F., Galbraith, D., Gilpin, M., Gloor, E., Grace, J., Hamer, K., Harris, D., Jeffery, K., Jucker, T., Kalamandeen, M., Klitgaard, B., Levesley, A., Lewis, S.L., Lindsell, J., Lopez-Gonzalez, G., Lovett, J., Malhi, Y., Matthews, T., McIntosh, E., Melgaço, K., Milliken, W., Mitchard, E., Moonlight, P., Moore, S., Morel, A., Peacock, J., Peh, K.S.-H., Pendry, C., Pennington, R.T., De Oliveira Pereira, L., Peres, C., Phillips, O.L., Pickavance, G., Pugh, T., Qie, L., Riutta, T., Roucoux, K., Ryan, C., Sarkinen, T., Valeria, C.S., Spracklen, D., Stas, S., Sullivan, M., Swaine, M., Talbot, J., Taplin, J., Van Der Heijden, G., Vedovato, L., Willcock, S., Williams, M., Alves, L., Loayza, P.A., Arellano, G., Asa, C., Ashton, P., Asner, G., Brncic, T., Brown, F., Burnham, R., Clark, C., Comiskey, J., Damasco, G., Davies, S., Di Fiore, T., Erwin, T., Farfan-Rios, W., Hall, J., Kenfack, D., Lovejoy, T., Martin, R., Montiel, O. M., Pipoly, J., Pitman, N., Poulsen, J., Primack, R., Silman, M., Steininger, M., Swamy, V., Terborgh, J., Thomas, D., Umunay, P., Uriarte, M., Torre, E.V., Wang, O., Young, K., Aymard, C.G.A., Hernández, L., Fernández, R.H., Ramírez-Angulo, H., Salcedo, P., Sanoja, E., Serrano, J., Torres-Lezama, A., Le, T.C., Le, T.T., Tran, H.D., 2021. Taking the pulse of Earth's tropical forests using networks of highly distributed plots. Biol. Conserv. 260, 108849. https://doi.org/10.1016/j.biocon.2020.108849.

Bouvet, A., Mermoz, S., Le Toan, T., Villard, L., Mathieu, R., Naidoo, L., Asner, G.P., 2018. An above-ground biomass map of African savannahs and woodlands at 25 m resolution derived from ALOS PALSAR. Remote Sens. Environ. 206, 156–173. https://doi.org/10.1016/j.rse.2017.12.030.

Cartus, O., Santoro, M., Kellndorfer, J., 2012. Mapping forest aboveground biomass in the Northeastern United States with ALOS PALSAR dual-polarization L-band. Remote Sens. Environ. 124, 466–478. https://doi.org/10.1016/j.rse.2012.05.029.

Cartus, O., Santoro, M., Wegmüller, U., Rommen, B., 2019. Benchmarking the retrieval of biomass in boreal forests using P-band SAR backscatter with multi-temporal C- and L-band observations. Remote Sens. 11, 1695. https://doi.org/10.3390/rs11141695.

Chauhan, N.S., Lang, R.H., Ranson, K.J., 1991. Radar modeling of a boreal forest. IEEE Trans. Geosci. Remote Sens. 29, 627–638.

Chave, J., Davies, S.J., Phillips, O.L., Lewis, S.L., Sist, P., Schepaschenko, D., Armston, J., Baker, T.R., Coomes, D., Disney, M., Duncanson, L., Hérault, B., Labrière, N., Meyer, V., Réjou-Méchain, M., Scipal, K., Saatchi, S., 2019. Ground data are essential for biomass remote sensing missions. Surv. Geophys. 40, 863–880. https://doi.org/10.1007/s10712-019-09528-w.

Chen, F., Guo, F., Liu, L., Nan, Y., 2021. An improved method for pan-tropical above-ground biomass and canopy height retrieval using CYGNSS. Remote Sens 13, 2491. https://doi.org/10.3390/rs13132491.

Coomes, D.A., Dalponte, M., Jucker, T., Asner, G.P., Banin, L.F., Burslem, D.F.R.P., Lewis, S.L., Nilus, R., Phillips, O.L., Phua, M.-H., Qie, L., 2017. Area-based vs tree-centric approaches to mapping forest carbon in Southeast Asian forests from airborne laser scanning data. Remote Sens. Environ. 194, 77–88. https://doi.org/10.1016/j.rse.2017.03.017.

Dalponte, M., Jucker, T., Liu, S., Frizzera, L., Gianelle, D., 2019. Characterizing forest carbon dynamics using multi-temporal lidar data. Remote Sens. Environ. 224, 412–420. https://doi.org/10.1016/j.rse.2019.02.018.

Davies, S.J., Abiem, I., Abu Salim, K., Aguilar, S., Allen, D., Alonso, A., Anderson-Teixeira, K., Andrade, A., Arellano, G., Ashton, P.S., Baker, P.J., Baker, M.E., Baltzer, J.L., Basset, Y., Bissiengou, P., Bohlman, S., Bourg, N.A., Brockelman, W.Y., Bunyavejchewin, S., Burslem, D.F.R.P., Cao, M., Cárdenas, D., Chang, L.-W., Chang-Yang, C.-H., Chao, K.-J., Chao, W.-C., Chapman, H., Chen, Y.-Y., Chisholm, R.A., Chu, C., Chuyong, G., Clay, K., Comita, L.S., Condit, R., Cordell, S., Dattaraja, H.S., De Oliveira, A.A., Den Ouden, J., Detto, M., Dick, C., Du, X., Duque, Á., Ediriweera, S., Ellis, E.C., Obiang, N.L.E., Esufali, S., Ewango, C.E.N., Fernando, E.S., Filip, J., Fischer, G.A., Foster, R., Giambelluca, T., Giardina, C., Gilbert, G.S., Gonzalez-Akre, E., Gunatilleke, I.A.U.N., Gunatilleke, C.V.S., Hao, Z., Hau, B.C.H., He, F., Ni, H., Howe, R.W., Hubbell, S.P., Huth, A., Inman-Narahari, F., Itoh, A., Janík, D., Jansen, P.A., Jiang, M., Johnson, D.J., Jones, F.A., Kanzaki, M., Kenfack, D., Kiratiprayoon, S., Král, K., Krizel, L., Lao, S., Larson, A.J., Li, Y., Li, X., Litton, C.M., Liu, Y., Liu, S., Lum, S.K.Y., Luskin, M.S., Lutz, J.A., Luu, H.T., Ma, K., Makana, J.-R., Malhi, Y., Martin, A., McCarthy, C., McMahon, S.M., McShea, W.J., Memiaghe, H., Mi, X., Mitre, D., Mohamad, M., Monks, L., Muller-Landau, H.C., Musili, P.M., Myers, J.A., Nathalang, A., Ngo, K.M., Norden, N., Novotny, V., O'Brien, M.J., Orwig, D., Ostertag, R., Papathanassiou, K., Parker, G.G., Pérez, R., Perfecto, I., Phillips, R.P., Pongpattananurak, N., Pretzsch, H., Ren, H., Reynolds, G., Rodriguez, L.J., Russo, S.E., Sack, L., Sang, W., Shue, J., Singh, A., Song, G.-Z.M., Sukumar, R., Sun, I.-F., Suresh, H.S., Swenson, N.G., Tan, S., Thomas, S.C., Thomas, D., Thompson, J., Turner, B.L., Uowolo, A., Uriarte, M., Valencia, R., Vandermeer, J., Vicentini, A., Visser, M., Vrska, T., Wang, Xugao, Wang, Xihua, Weiblen, G.D., Whitfeld, T.J.S., Wolf, A., Wright, S.J., Xu, H., Yao, T.L., Yap, S.L., Ye, W., Yu, M., Zhang, M., Zhu, D., Zhu, L., Zimmerman, J.K., Zuleta, D., 2021. ForestGEO: understanding forest diversity and dynamics through a global observatory network. Biol. Conserv. 253, 108907. https://doi.org/10.1016/j.biocon.2020.108907.

Defourny, P., Moreau, I., Bontemps, S., Lamarche, C., Brockmann, C., Boettcher, M., Wevers, J., Kirches, G., Santoro, M., 2017. Land Cover CCI, Product User Guide. No. Version 2.0).

DiMiceli, C.M., Carroll, M.L., Sohlberg, R.A., Huang, C., Hansen, M.C., Townshend, J.R. G., 2011. Annual Global Automated MODIS Vegetation Continuous Fields (MOD44B) at 250 M Spatial Resolution for Data Years Beginning Day 65, 2000 - 2010, Collection 5 Percent Tree Cover.

Duncanson, L., Kellner, J.R., Armston, J., Dubayah, R., Minor, D.M., Hancock, S., Healey, S.P., Patterson, P.L., Saarela, S., Marselis, S., Silva, C.E., Bruening, J., Goetz, S.J., Tang, H., Hofton, M., Blair, B., Luthcke, S., Fatoyinbo, L., Abernethy, K., Alonso, A., Andersen, H.-E., Aplin, P., Baker, T.R., Barbier, N., Bastin, J.F., Biber, P., Boeckx, P., Bogaert, J., Boschetti, L., Boucher, P.B., Boyd, D.S., Burslem, D.F.R.P., Calvo-Rodriguez, S., Chave, J., Chazdon, R.L., Clark, D.B., Clark, D.A., Cohen, W.B., Coomes, D.A., Corona, P., Cushman, K.C., Cutler, M.E.J., Dalling, J.W., Dalponte, M., Dash, J., de-Miguel, S., Deng, S., Ellis, P.W., Erasmus, B., Fekety, P.A., Fernandez-Landa, A., Ferraz, A., Fischer, R., Fisher, A.G., García-Abril, A., Gobakken, T., Hacker, J.M., Heurich, M., Hill, R.A., Hopkinson, C., Huang, H., Hubbell, S.P., Hudak, A.T., Huth, A., Imbach, B., Jeffery, K.J., Katoh, M., Kearsley, E., Kenfack, D., Kljun, N., Knapp, N., Král, K., Krůček, M., Labrière, N., Lewis, S.L., Longo, M., Lucas, R.M., Main, R., Manzanera, J.A., Martínez, R.V., Mathieu, R., Memiaghe, H., Meyer, V., Mendoza, A.M., Monerris, A., Montesano, P., Morsdorf, F., Næsset, E., Naidoo, L., Nilus, R., O'Brien, M., Orwig, D.A., Papathanassiou, K., Parker, G., Philipson, C., Phillips, O.L., Pisek, J., Poulsen, J.R., Pretzsch, H., Rüdiger, C., Saatchi, S., Sanchez-Azofeifa, A., Sanchez-Lopez, N., Scholes, R., Silva, C.A., Simard, M., Skidmore, A., Stereńczak, K., Tanase, M., Torresan, C., Valbuena, R., Verbeeck, H., Vrska, T., Wessels, K., White, J.C., White, L.J.T., Zahabu, E., Zgraggen, C., 2022. Aboveground biomass density models for NASA's Global Ecosystem Dynamics Investigation (GEDI) lidar mission. Remote Sens. Environ. 270, 112845. https://doi.org/10.1016/j.rse.2021.112845.

Fahrland, E., 2022. Copernicus DEM Product Handbook (No. Date: 3 June 2022, Version 4.0).

Fan, L., Wigneron, J.-P., Ciais, P., Chave, J., Brandt, M., Fensholt, R., Saatchi, S.S., Bastos, A., Al-Yaari, A., Hufkens, K., Qin, Y., Xiao, X., Chen, C., Myneni, R.B., Fernandez-Moran, R., Mialon, A., Rodriguez-Fernandez, N.J., Kerr, Y., Tian, F., Peñuelas, J., 2019. Satellite-observed pantropical carbon dynamics. Nat. Plants 5, 944–951. https://doi.org/10.1038/s41477-019-0478-9.

FAO, 2020. Global Forest Resources Assessment 2020. Rome.

Ferraz, A., Saatchi, S., Xu, L., Hagen, S., Chave, J., Yu, Y., Meyer, V., Garcia, M., Silva, C., Roswintiart, O., Samboko, A., Sist, P., Walker, S., Pearson, T.R.H., Wijaya, A., Sullivan, F.B., Rutishauser, E., Hoekman, D., Ganguly, S., 2018. Carbon storage potential in degraded forests of Kalimantan, Indonesia. Environ. Res. Lett. 13, 095001. https://doi.org/10.1088/1748-9326/aad782.

Frey, O., Santoro, M., Werner, C.L., Wegmuller, U., 2013. DEM-based SAR pixel-area estimation for enhanced geocoding refinement and radiometric normalization. IEEE Geosci. Remote Sens. Lett. 10, 48–52. https://doi.org/10.1109/LGRS.2012.2192093.

Goetz, S.J., Baccini, A., Laporte, N.T., Johns, T., Walker, W., Kellndorfer, J., Houghton, R.A., Sun, M., 2009. Mapping and monitoring carbon stocks with satellite observations: a comparison of methods. Carbon Balance Manag 4. https://doi.org/10.1186/1750-0680-4-2.

Hansen, M.C., Potapov, P.V., Moore, R., Hancher, M., Turubanova, S.A., Tyukavina, A., Thau, D., Stehman, S.V., Goetz, S.J., Loveland, T.R., Kommareddy, A., Egorov, A., Chini, L., Justice, C.O., Townshend, J.R.G., 2013. High-resolution global maps of 21-st century forest cover change. Science 342, 850–853. https://doi.org/10.1126/science.1244693.

Hofton, M.A., Minster, J.B., Blair, J.B., 2000. Decomposition of laser altimeter waveforms. IEEE Trans. Geosci. Remote Sens. 38, 1989–1996. https://doi.org/10.1109/36.851780.

Houghton, R.A., Hall, F., Goetz, S.J., 2009. Importance of forest biomass in the global carbon cycle. J. Geophys. Res. 114, G00E03. https://doi.org/10.1029/2009JG000935.

Hu, T., Su, Y., Xue, B., Liu, J., Zhao, X., Fang, J., Guo, Q., 2016. Mapping global forest aboveground biomass with spaceborne LiDAR, optical imagery, and forest inventory data. Remote Sens 8, 565. https://doi.org/10.3390/rs8070565.

Hunka, N., Santoro, M., Armston, J., Dubayah, R., McRoberts, R.E., Næsset, E., Quegan, S., Urbazaev, M., Pascual, A., May, P.B., Minor, D., Leitold, V., Basak, P., Liang, M., Melo, J., Herold, M., Málaga, N., Wilson, S., Durán Montesinos, P., Arana, A., Ernesto De La Cruz Paiva, R., Ferrand, J., Keoka, S., Guerra-Hernández, J., Duncanson, L., 2023. On the NASA GEDI and ESA CCI biomass maps: aligning for uptake in the UNFCCC global stocktake. Environ. Res. Lett. 18, 124042. https://doi.org/10.1088/1748-9326/ad0b60.

Kay, H., Santoro, M., Cartus, O., Bunting, P., Lucas, R., 2021. Exploring the relationship between forest canopy height and canopy density from spaceborne LiDAR observations. Remote Sens 13, 4961. https://doi.org/10.3390/rs13244961.

Keller, M., Duffy, P., Barnett, W., 2019. LiDAR and PALSAR-derived forest aboveground biomass, paragominas, para, Brazil, 2012 23.291921 MB. https://doi.org/10.3334/ORNLDAAC/1648.

Kurum, M., Lang, R.H., O'Neill, P.E., Joseph, A.T., Jackson, T.J., Cosh, M.H., 2009. L-Band radar estimation of forest attenuation for active/passive soil moisture inversion. IEEE Trans. Geosci. Remote Sens. 47, 3026–3040.

Kurvonen, L., Pulliainen, J., Hallikainen, M., 1999. Retrieval of biomass in boreal forests from multitemporal ERS-1 and JERS-1 SAR images. IEEE Trans. Geosci. Remote Sens. 37, 198–205. https://doi.org/10.1109/36.739154.

Labrière, N., Davies, S.J., Disney, M.I., Duncanson, L.I., Herold, M., Lewis, S.L., Phillips, O.L., Quegan, S., Saatchi, S.S., Schepaschenko, D.G., Scipal, K., Sist, P., Chave, J., 2023. Toward a forest biomass reference measurement system for remote sensing applications. Glob. Change Biol. 29, 827–840. https://doi.org/10.1111/gcb.16497.

Labriere, N., Tao, S., Chave, J., Scipal, K., Toan, T.L., Abernethy, K., Alonso, A., Barbier, N., Bissiengou, P., Casal, T., Davies, S.J., Ferraz, A., Herault, B., Jaouen, G., Jeffery, K.J., Kenfack, D., Korte, L., Lewis, S.L., Malhi, Y., Memiaghe, H.R., Poulsen, J.R., Rejou-Mechain, M., Villard, L., Vincent, G., White, L.J.T., Saatchi, S., 2018. In situ reference datasets from the TropiSAR and AfriSAR campaigns in support of upcoming spaceborne biomass missions. IEEE J. Sel. Top. Appl. Earth Obs. Remote Sens. 11, 3617–3627. https://doi.org/10.1109/JSTARS.2018.2851606.

Lang, N., Kalischek, N., Armston, J., Schindler, K., Dubayah, R., Wegner, J.D., 2022. Global canopy height regression and uncertainty estimation from GEDI LIDAR waveforms with deep ensembles. Remote Sens. Environ. 268, 112760. https://doi.org/10.1016/j.rse.2021.112760.

Liu, Y.Y., van Dijk, A.I.J.M., de Jeu, R.A.M., Canadell, J.G., McCabe, M.F., Evans, J.P., Wang, G., 2015. Recent reversal in loss of global terrestrial biomass. Nat. Clim. Change 5, 470–474. https://doi.org/10.1038/nclimate2581.

Los, S.O., Rosette, J.A.B., Kljun, N., North, P.R.J., Chasmer, L., Suárez, J.C., Hopkinson, C., Hill, R.A., Van Gorsel, E., Mahoney, C., Berni, J.A.J., 2012. Vegetation height and cover fraction between 60° S and 60° N from ICESat GLAS data. Geosci. Model Dev. (GMD) 5, 413–432. https://doi.org/10.5194/gmd-5-413-2012.

Markus, T., Neumann, T., Martino, A., Abdalati, W., Brunt, K., Csatho, B., Farrell, S., Fricker, H., Gardner, A., Harding, D., Jasinski, M., Kwok, R., Magruder, L., Lubin, D., Luthcke, S., Morison, J., Nelson, R., Neuenschwander, A., Palm, S., Popescu, S., Shum, C., Schutz, B.E., Smith, B., Yang, Y., Zwally, J., 2017. The ice, cloud, and land elevation satellite-2 (ICESat-2): science requirements, concept, and implementation. Remote Sens. Environ. 190, 260–273. https://doi.org/10.1016/j.rse.2016.12.029.

Milenković, M., Reiche, J., Armston, J., Neuenschwander, A., De Keersmaecker, W., Herold, M., Verbesselt, J., 2022. Assessing Amazon rainforest regrowth with GEDI and ICESat-2 data. Sci. Remote Sens. 5, 100051. https://doi.org/10.1016/j.srs.2022.100051.

Mitchard, E.T.A., Saatchi, S.S., Baccini, A., Asner, G.P., Goetz, S.J., Harris, N.L., Brown, S., 2013. Uncertainty in the spatial distribution of tropical forest biomass: a comparison of pan-tropical maps. Carbon Balance Manag 8, 1. https://doi.org/10.1186/1750-0680-8-10.

Neuenschwander, A., Pitts, K., 2019. The ATL08 land and vegetation product for the ICESat-2 Mission. Remote Sens. Environ. 221, 247–259.

Neuenschwander, A.L., Urban, T.J., Gutierrez, R., Schutz, B.E., 2008. Characterization of ICESat/GLAS waveforms over terrestrial ecosystems: implications for vegetation mapping. J. Geophys. Res. Biogeosciences 113, 2007JG000557. https://doi.org/10.1029/2007JG000557.

Oliver, C., Quegan, S., 1998. Understanding Synthetic Aperture Radar Images. Artech House, Boston.

Olson, D.M., Dinerstein, E., Wikramanayake, E.D., Burgess, N.D., Powell, G.V.N., Underwood, E.C., D'amico, J.A., Itoua, I., Strand, H.E., Morrison, J.C., Loucks, C.J., Allnutt, T.F., Ricketts, T.H., Kura, Y., Lamoreux, J.F., Wettengel, W.W., Hedao, P., Kassem, K.R., 2001. Terrestrial ecoregions of the world: a New map of Life on earth. Bioscience 51, 933. https://doi.org/10.1641/0006-3568(2001)051[0933:TEOTWA]2.0.CO;2.

Ometto, J.P., Gorgens, E.B., De Souza Pereira, F.R., Sato, L., De Assis, M.L.R., Cantinho, R., Longo, M., Jacon, A.D., Keller, M., 2023. A biomass map of the Brazilian Amazon from multisource remote sensing. Sci. Data 10, 668. https://doi.org/10.1038/s41597-023-02575-4.

Plummer, S., Lecomte, P., Doherty, M., 2017. The ESA climate change initiative (CCI): a European contribution to the generation of the global climate observing system. Remote Sens. Environ. 203, 2–8. https://doi.org/10.1016/j.rse.2017.07.014.

Potapov, P., Li, X., Hernandez-Serna, A., Tyukavina, A., Hansen, M.C., Kommareddy, A., Pickens, A., Turubanova, S., Tang, H., Silva, C.E., Armston, J., Dubayah, R., Blair, J. B., Hofton, M., 2021. Mapping global forest canopy height through integration of GEDI and Landsat data. Remote Sens. Environ. 253, 112165. https://doi.org/10.1016/j.rse.2020.112165.

Praks, J., Antropov, O., Hallikainen, M., 2012. LIDAR-aided SAR interferometry studies in boreal forest: scattering phase center and extinction coefficient at X- and L-band. Remote Sens 50, 3831–3843.

Prigent, C., Jimenez, C., 2021. An evaluation of the synergy of satellite passive microwave observations between 1.4 and 36 GHz, for vegetation characterization over the Tropics. Remote Sens. Environ. 257, 112346. https://doi.org/10.1016/j.rse.2021.112346.

Réjou-Méchain, M., Barbier, N., Couteron, P., Ploton, P., Vincent, G., Herold, M., Mermoz, S., Saatchi, S., Chave, J., De Boissieu, F., Féret, J.-B., Takoudjou, S.M., Pélissier, R., 2019. Upscaling forest biomass from field to satellite measurements: sources of errors and ways to reduce them. Surv. Geophys. 40, 881–911. https://doi.org/10.1007/s10712-019-09532-0.

Réjou-Méchain, M., Muller-Landau, H.C., Detto, M., Thomas, S.C., Le Toan, T., Saatchi, S. S., Barreto-Silva, J.S., Bourg, N.A., Bunyavejchewin, S., Butt, N., Brockelman, W.Y., Cao, M., Cárdenas, D., Chiang, J.-M., Chuyong, G.B., Clay, K., Condit, R., Dattaraja, H.S., Davies, S.J., Duque, A., Esufali, S., Ewango, C., Fernando, R.H.S., Fletcher, C.D., Gunatilleke, I.A.U.N., Hao, Z., Harms, K.E., Hart, T.B., Hérault, B., Howe, R.W., Hubbell, S.P., Johnson, D.J., Kenfack, D., Larson, A.J., Lin, L., Lin, Y., Lutz, J.A., Makana, J.-R., Malhi, Y., Marthews, T.R., McEwan, R.W., McMahon, S.M., McShea, W.J., Muscarella, R., Nathalang, A., Noor, N.S.M., Nytch, C.J., Oliveira, A. A., Phillips, R.P., Pongpattananurak, N., Punchi-Manage, R., Salim, R., Schurman, J., Sukumar, R., Suresh, H.S., Suwanvecho, U., Thomas, D.W., Thompson, J., Uríarte, M., Valencia, R., Vicentini, A., Wolf, A.T., Yap, S., Yuan, Z., Zartman, C.E., Zimmerman, J.K., Chave, J., 2014. Local spatial structure of forest biomass and its consequences for remote sensing of carbon stocks. Biogeosciences 11, 6827–6840. https://doi.org/10.5194/bg-11-6827-2014.

Rodríguez-Fernández, N.J., Mialon, A., Mermoz, S., Bouvet, A., Richaume, P., Al Bitar, A., Al-Yaari, A., Brandt, M., Kaminski, T., Le Toan, T., Kerr, Y.H., Wigneron, J.-P., 2018. An evaluation of SMOS L-band vegetation optical depth (L-VOD) data sets: high sensitivity of L-VOD to above-ground biomass in Africa. Biogeosciences 15, 4627–4645. https://doi.org/10.5194/bg-15-4627-2018.

Rosenqvist, A., Shimada, M., Suzuki, S., Ohgushi, F., Tadono, T., Watanabe, M., Tsuzuku, K., Watanabe, T., Kamijo, S., Aoki, E., 2014. Operational performance of the ALOS global systematic acquisition strategy and observation plans for ALOS-2 PALSAR-2. Remote Sens. Environ. 155, 3–12. https://doi.org/10.1016/j.rse.2014.04.011.

Saatchi, S.S., Harris, N.L., Brown, S., Lefsky, M., Mitchard, E.T.A., Salas, W., Zutta, B.R., Buermann, W., Lewis, S.L., Hagen, S., Petrova, S., White, L., Silman, M., Morel, A., 2011. Benchmark map of forest carbon stocks in tropical regions across three continents. Proc. Natl. Acad. Sci. 108, 9899–9904. https://doi.org/10.1073/pnas.1019576108.

Salazar-Neira, J.C., Mialon, A., Richaume, P., Mermoz, S., Kerr, Y.H., Bouvet, A., Le Toan, T., Boitard, S., Rodríguez-Fernández, N.J., 2023. Above-ground biomass estimation based on multi-angular L -band measurements of brightness temperatures. IEEE J. Sel. Top. Appl. Earth Obs. Remote Sens. 16, 5813–5827. https://doi.org/10.1109/JSTARS.2023.3285288.

Santoro, M., Askne, J., Smith, G., Fransson, J.E.S., 2002. Stem volume retrieval in boreal forests from ERS-1/2 interferometry. Remote Sens. Environ. 81, 19–35. https://doi.org/10.1016/S0034-4257(01)00329-7.

Santoro, M., Beer, C., Cartus, O., Schmullius, C., Shvidenko, A., McCallum, I., Wegmüller, U., Wiesmann, A., 2011. Retrieval of growing stock volume in boreal forest using hyper-temporal series of Envisat ASAR ScanSAR backscatter measurements. Remote Sens. Environ. 115, 490–507. https://doi.org/10.1016/j.rse.2010.09.018.

Santoro, M., Cartus, O., 2018. Research pathways of forest above-ground biomass estimation based on SAR backscatter and interferometric SAR observations. Remote Sens 10, 608. https://doi.org/10.3390/rs10040608.

Santoro, M., Cartus, O., Carvalhais, N., Rozendaal, D., Avitabilie, V., Araza, A., de Bruin, S., Herold, M., Quegan, S., Rodríguez Veiga, P., Balzter, H., Carreiras, J., Schepaschenko, D., Korets, M., Shimada, M., Itoh, T., Moreno Martínez, Á., Cavlovic, J., Cazzolla Gatti, R., da Conceição Bispo, P., Dewnath, N., Labrière, N., Liang, J., Lindsell, J., Mitchard, E.T.A., Morel, A., Pacheco Pascagaza, A.M., Ryan, C. M., Slik, F., Vaglio Laurin, G., Verbeeck, H., Wijaya, A., Willcock, S., 2021a. The global forest above-ground biomass pool for 2010 estimated from high-resolution satellite observations. Earth Syst. Sci. Data 13, 3927–3950. https://doi.org/10.5194/essd-2020-148.

Santoro, M., Cartus, O., Fransson, J.E.S., 2021b. Integration of allometric equations in the water cloud model towards an improved retrieval of forest stem volume with L-band SAR data in Sweden. Remote Sens. Environ. 253, 112235. https://doi.org/10.1016/j.rse.2020.112235.

Santoro, M., Cartus, O., Wegmüller, U., Besnard, S., Carvalhais, N., Araza, A., Herold, M., Liang, J., Cavlovic, J., Engdahl, M.E., 2022. Global estimation of above-ground biomass from spaceborne C-band scatterometer observations aided by LiDAR metrics of vegetation structure. Remote Sens. Environ. 279, 113114. https://doi.org/10.1016/j.rse.2022.113114.

Santoro, M., Wegmüller, U., Lamarche, C., Bontemps, S., Defourny, P., Arino, O., 2015. Strengths and weaknesses of multi-year Envisat ASAR backscatter measurements to map permanent open water bodies at global scale. Remote Sens. Environ. 171, 185–201. https://doi.org/10.1016/j.rse.2015.10.031.

Sheen, D.R., Malinas, N.P., Kletzli, D.W., Lewis, T.B., Roman, J.F., 1994. Foliage transmission measurements using a ground-based ultrawide band (300-1300 MHz) SAR system. IEEE Trans. Geosci. Remote Sens. 32, 118–130.

Shendryk, Y., 2022. Fusing GEDI with earth observation data for large area aboveground biomass mapping. Int. J. Appl. Earth Obs. Geoinformation 115, 103108. https://doi.org/10.1016/j.jag.2022.103108.

Shimada, M., Ohtaki, T., 2010. Generating large-scale high-quality SAR mosaic datasets: application to PALSAR data for global monitoring. IEEE J. Sel. Top. Appl. Earth Obs. Remote Sens. 3, 637–656.

Shinohara, H., Homma, T., Nohmi, H., Hirosawa, H., Tagawa, T., 1992. Relation between L-band microwave penetration/backscattering characteristics and state of trees. In: IGARSS'92. IEEE Publications, Piscataway, NJ, pp. 539–541.

Simard, M., Pinto, N., Fisher, J.B., Baccini, A., 2011. Mapping forest canopy height globally with spaceborne LiDAR. J. Geophys. Res. 116. https://doi.org/10.1029/2011JG001708.

Tadono, T., Ishida, H., Oda, F., Naito, S., Minakawa, K., Iwamoto, H., 2014. Precise global DEM generation by ALOS PRISM. ISPRS Ann. Photogramm. Remote Sens. Spat. Inf. Sci. II–4, 71–76. https://doi.org/10.5194/isprsannals-II-4-71-2014.

Ulaby, F.T., Whitt, M.W., Dobson, M.C., 1990. Measuring the propagation properties of a forest canopy using a polarimetric scatterometer. IEEE Trans. Antennas Propag. 38, 251–258.

Walker, W.S., Kellndorfer, J.M., LaPoint, E., Hoppus, M., Westfall, J., 2007. An empirical InSAR-optical fusion approach to mapping vegetation canopy height. Remote Sens. Environ. 109, 482–499.

Wegmüller, U., 1999. Automated terrain corrected SAR geocoding. In: IGARSS'99. IEEE Publications, Piscataway, NJ, pp. 1712–1714.

Wegmüller, U., Werner, C., Strozzi, T., Wiesmann, A., 2002. Automated and precise image registration procedures. In: Bruzzone, Smits (Ed.), Analysis of Multi-Temporal Remote Sensing Images, Series in Remote Sensing. World Scientific, Trento, pp. 37–49, 13-14 September 2001.

Xu, L., Saatchi, S.S., Shapiro, A., Meyer, V., Ferraz, A., Yang, Y., Bastin, J.-F., Banks, N., Boeckx, P., Verbeeck, H., Lewis, S.L., Muanza, E.T., Bongwele, E., Kayembe, F., Mbenza, D., Kalau, L., Mukendi, F., Ilunga, F., Ebuta, D., 2017. Spatial distribution of carbon stored in forests of the democratic republic of Congo. Sci. Rep. 7. https://doi.org/10.1038/s41598-017-15050-z.

Xu, L., Saatchi, S.S., Yang, Y., Yu, Y., Pongratz, J., Bloom, A.A., Bowman, K., Worden, J., Liu, J., Yin, Y., Domke, G., McRoberts, R.E., Woodall, C., Nabuurs, G.-J., de-Miguel, S., Keller, M., Harris, N., Maxwell, S., Schimel, D., 2021. Changes in global terrestrial live biomass over the 21st century. Sci. Adv. 7, eabe9829. https://doi.org/10.1126/sciadv.abe9829.